Ultrafast X-ray Absorption Spectroscopy

Christian Bressler and Majed Chergui*

Laboratoire de Spectroscopie Ultrarapide, ISIC-FSB-BSP, Ecole Polytechnique Fédérale de Lausanne, CH-1015 Lausanne, Switzerland

Received September 22, 2003

Contents

* Corresponding author. E-mail: Majed.Chergui@epfl.ch.

1. Introduction

The development of femtosecond lasers brought entirely new possibilities into the practice of time-resolved spectroscopy, for both UV−vis and IR−Raman spectroscopies. In addition, it has boosted the capabilities of nonlinear spectroscopies beyond what could be imagined before their advent. The implementation of femtosecond laser spectroscopies for the study of molecular phenomena and, in particular, of chemical reactions has given birth to the field of femtochemistry.[1] Indeed, for the first time, it became possible to conduct observations on time scales that are shorter than single nuclear oscillation periods in molecules. It therefore became possible, in principle, to monitor molecules at various stages of vibrational distortion, recording "stop-action" spectroscopic events corresponding to well-defined molecular geometries far from equilibrium,[2,3] including stretched and/or bent unstable transient structures. Molecular structures corresponding to such unstable intermediates between reactant and product could be followed in real-time.[1] This approach is not limited to molecules, and in principle, distorted crystal lattices and other specific out-of-equilibrium structures have been characterized.[4]

The realization of these experimental possibilities requires not only adequate time resolution for probing vibrations but also excitation mechanisms suitable for initiating molecular motion in a phase-coherent (i.e., synchronized) manner in order to "observe" the transient structures.[5] The typical approach for recording molecular motion in real-time is based on the pump−probe scheme depicted in Figure 1. Absorption of a first pulse of light (called the pump pulse, Figure 1a) brings the molecule from the ground-state potential V_1 to the excited-state potential V_2 (Figure 1b). If the pulse is sufficiently short in time (and at least shorter than the oscillation period of the molecule in the excited-state V_2), then a coherent superposition of vibrational levels (a so-called wave packet) is created, which is localized in space at the ground state equilibrium configuration at time $t = 0$. The newly created wave packet will feel the driving force of the excited state potential and will undergo oscillations at a frequency characteristic of the vibrational spacings of the excited state potential, if the latter is bound. Key issues here are the following: (a) the creation of a wave packet implies that all excited molecules in the irradiated volume have the same configuration within the spatial spread of the wave packet. Thus, the shorter

10.1021/cr0206667 CCC: $48.50
Published on Web 03/16/2004

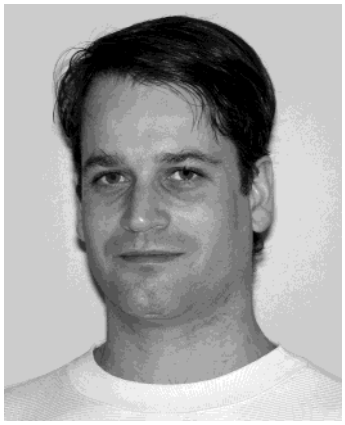

Christian Bressler was born 1964 in Knoxville, Tennessee, and grew up in the United States and Germany. He studied physics at the University of Heidelberg and obtained his diploma with a thesis on exotic atoms generated at the Rutherford Appleton Laboratory (RAL) near Oxford. He received his Ph.D. degree under the supervision of Prof. N. Schwentner at the Free University of Berlin in 1995, working on the spectroscopy and photomobility of matrix-isolated molecules and atoms with VUV synchrotron radiation at BESSY. He spent two years at SRI International in Menlo Park, California, investigating cryogenic high energy density matter and collisional quenching of electronically excited molecules. In 1998, he relocated to the group of Prof. M. Chergui at the University of Lausanne working on the implementation of ultrafast time-resolved structural dynamics at synchrotrons. In 2002, he became Assistant Professor of Physics at the University of Lausanne, and since 2003, he is an Assistant Professor of Physics at the Swiss Federal Institute of Technology in Lausanne. Over the past 5 years he has been working on time-resolved X-ray absorption spectroscopy with synchrotron radiation (ESRF–Grenoble, ALS–Berkeley, and SLS–Villigen) and laboratory-based pulsed X-ray sources. His current research interests focus on the application of ultrafast structural methods to the understanding of fundamental chemical reactions in the condensed phase.

Majed Chergui was born in 1956 in Casablanca, Morocco, and grew up in Algeria and Lebanon. He obtained his B.S. in physics and mathematics from King's College, London, in 1977, and a year later he obtained his M.S. in atomic and molecular physics from the Université Paris-sud, Orsay. He obtained his Ph.D. at the same university with a thesis on collisional quenching of electronically excited molecules under the supervision of the late V. Chandrasekharan. In 1982, he became research assistant at the CNRS and developed interest in the fate of Rydberg states of molecules in rare gas matrixes, which he studied using vacuum ultraviolet radiation at the synchrotron centers LURE (Orsay) and Hasylab (Hamburg). At the end of 1986, he obtained his habilitation and moved to Berlin as an Alexander von Humboldt Fellow at the Free University for two years. Then as research assistant in the group of Prof. N. Schwentner, he carried out matrix-isolation studies of photochemical reactions with synchrotron radiation and, later, resonance Raman studies of photochemical reactions in the liquid phase. In 1993, he was appointed Full Professor of Condensed Matter Physics at the Université de Lausanne, Switzerland. In 2003, he became Professor of Physics and Chemistry at the Swiss Federal Institute of Technology in Lausanne. His current research focuses on the fundamental aspects of photoinduced dynamics in condensed molecular media and in biological systems. He is also developing and using ultrafast X-ray techniques to probe structural dynamics in liquid systems.

the pump pulse, the sharper defined the distribution of molecular configurations will be. (b) The time evolution of the wave packet reflects that of the ensemble of coherently excited molecules, which evolve in phase.

The observation of molecular motion via the dynamics of the wave packet is done by using a second ultrashort laser pulse (called the probe pulse, Figure 1a) that interrogates the ensemble excited by the pump pulse and whose time delay with respect to the latter can be tuned. The probe pulse induces a transition between V_2 and a higher lying state V_3. The choice of the probe wavelength determines the choice of the probed configuration, as can be seen in Figure 1b. Thus, changing the probe wavelength allows the probing of different configurations. The spatial width of the window in real space, which is opened by the probe pulse, is determined by its spectral width and by the slope of the potential difference between V_2 and V_3. Each time the wave packet enters the probe window, a signal is detected, which can be the absorption of the probe pulse, a fluorescence signal from V_3 induced by the probe absorption, or an ion signal, if V_3 is an ion potential. The signal will appear modulated at the oscillation period of the wave packet (Figure 1c). The key point here is that the structural dynamics is retrieved from spectroscopic signals thanks to a knowledge of the energetics of the molecular system, i.e., its spectroscopy.

The pump−probe scheme has been a revolutionary tool to observe motion in real-time of bound states of small diatomic molecules, such as I_2,[6,7] NaI,[8] and Na_2,[9,10] and of elementary chemical reactions, such as the dissociation of ICN[3] and HgI_2,[11] to name a few. Its implementation (and variants of it) with the study of systems of even greater complexity occurred throughout the 1990s,[12−15] with the study of elementary reactions in gas-phase organic molecules,[1] in liquids,[16,17] in solids[4,18−22] and in biological molecules.[1,13,23] The major and clear-cut success of femtosecond pump−probe spectroscopies has established the field of femtochemistry as the core of physical chemistry, since it addresses the fundamental time scale at which molecular motion occurs.

While the relation between probe wavelength and probed configuration is a trivial one in the case of diatomic and some triatomic molecules (provided their steady-state spectroscopy has been established), this relationship becomes ambiguous as the molecular system increases in complexity and size. One may still circumvent these difficulties by combining steady-state spectroscopy and quantum-chemical calculations to help explain the dynamics obtained from femtosecond pump−probe studies. However, translating spectroscopic observables (transition energies and intensities) into molecular structure becomes a prohibitively difficult task. Extensions of the pump−probe scheme in combination with mass-spectrometry,[1] kinetic energy of electrons and or ions,[9] or pump−dump schemes[24] allow one to get a closer description of transient structures. A further degree

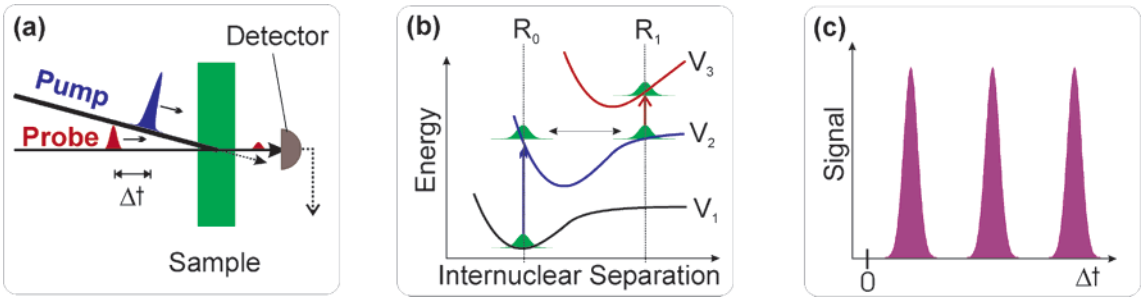

Figure 1. Principle of the pump−probe experiment: (a) A first laser (pump) pulse excites the sample at time $t = 0$. A second (probe) laser pulse, whose time delay Δt can be tuned with respect to the pump pulse, records the evolution of the system at a given configuration. (b) Schematic potential curve diagram of a molecular system. The pump pulse excites the system from the ground-state V_1 in its initial configuration R_0, to the first excited state V_2. The probe pulse samples the evolution of the wave packet created on the potential surface V_2, by inducing a transition from V_2 to V_3. The choice of the probe wavelength monitors the probed configuration R_1 as a function of time delay. Tuning the probe wavelength allows one to probe different configurations. The probe transition gives rise to a signal that can be the absorption of the probe photons, an emission following absorption into V_3, or an ion/electron signal, if V_3 lies above the ionization potential of the system. (c) The motion of the wave packet on surface V_2 appears in the form of an oscillatory signal, if V_2 is a bound state whose oscillation period reflects that of the vibrating molecule.

of complexity is added to the problem, if we are dealing with condensed phase or biological samples, since intermolecular coordinates come into play. Consequently, experimental approaches are needed that can overcome the limitations of optical studies for structural determination, while the high temporal resolution of femtosecond lasers is maintained.

Structural techniques such as X-ray diffraction, electron diffraction, X-ray absorption spectroscopy (XAS), and neutron scattering can deliver the answer, provided sufficiently short and intense pulses of X-rays, electrons, or neutrons can be produced. While neutrons are commonly used in the static regime, we are not aware of any work using them for time-resolved studies. The majority of time-resolved structural studies have been carried out with ultrashort pulses of X-rays or electrons, either using diffraction techniques or X-ray spectroscopies. Conceptually, the methods of ultrafast X-ray (and electron) diffraction and X-ray absorption are similar to ultrafast optical pump−probe experiments. The essential new ingredient is that the probe is not optical but via an X-ray (or electron) pulse that is diffracted or absorbed (for X-ray absorption only).

An impressive effort over the last 12 years has recently culminated in the demonstration of the feasibility of ultrafast electron diffraction, where transient structures of molecules in the gas phase, including molecules containing low-Z atoms, have been determined with picosecond temporal resolution.[25−36] The key point to the success of electron diffraction lies in the high scattering cross sections of electrons, which is 5 orders of magnitude larger than that for X-rays. The fact that the energy deposited per scattering event is 2−3 orders of magnitude weaker is certainly attractive in view of destruction by the probe beam. Extending time-resolved electron diffraction to condensed phases would be a major challenge, due to the low penetration depth of electrons in matter, and the technique will most probably have success in the study of surface phenomena.

X-ray techniques using diffraction or absorption, on the other hand, offer the advantage of high penetration depth in matter. This review concentrates on the techniques of ultrafast X-ray absorption spectroscopy. However, to appreciate the advantages and limitations with respect to X-ray diffraction techniques, we will also briefly review the latter.

2. X-ray Diffraction

Since the beginning of the 20th century, X-rays have been used to determine not only the equilibrium structure of crystalline materials[37,38] but also the electron density of a large number of small molecules, as well as many important biomolecules and biopolymers.[37−39] This is possible thanks to the clear and well-established connection between atomic positions and the scattering amplitudes of X-rays, via a Fourier relation.[37−39] With this in mind, it has been proposed that X-ray diffraction may be used to directly watch structural changes and atomic motions during chemical (and biochemical) reactions or physical processes (e.g. phase transitions and order−disorder phenomena).[40−43]

In crystals, atoms are arranged in periodic lattices. The incident X-rays experience a three-dimensional arrangement of the electron density. In the direction of constructive interference, a well-defined pattern of scattered X-ray intensities is observed, which satisfies Bragg's law for diffraction:

$$2d_{ijk} \sin \Theta = \lambda \qquad (1)$$

where λ is the X-ray wavelength, d_{ijk} is the crystal plane spacing, and Θ is the angle of incidence between the X-ray beam and the selected lattice plane. By rotating the crystal, different sets of diffracting planes can be studied (Bragg diffraction). When polychromatic X-radiation is used, the crystal may remain stationary and it will select and diffract radiation of different wavelengths in different directions in order to satisfy Bragg's law. This method, known as Laue diffraction, makes possible the collection of diffracted data from many different lattice planes simultaneously.

In the case of noncrystalline materials, such as amorphous media, liquids, and gases, where there is an absence of periodic arrangement of atoms or

molecules, X-ray diffraction is much less efficient. Nevertheless, it was already demonstrated for gaseous samples back in 1929, when Debye and Ehrhardt[44] imaged the scattering pattern of carbon tetrachloride vapor, obtaining information on its molecular structure. The average intensity of the scattered X-rays from an assembly of atoms is determined by the Debye equation:

$$I_a = \sum_m \sum_n f_m f_n \frac{\sin kr_{mn}}{kr_{mn}} \quad (2)$$

where the f's represent the scattering amplitudes of the m,n atoms, $k = 4\pi \sin \Theta/\lambda$, r_{mn} is the distance between the mth and the nth atom, and Θ is the scattering angle. Since there is a relative structure at short range around the center of an average atom, it is expressed in the form of a radial distribution function. Modulation of the radial distribution function can deliver information about interatomic distances and molecular structure in liquids and amorphous solids.

Ultrafast time-resolved diffraction has been used only since the past 5−10 years. Most studies have dealt with issues of material science, such as the dynamics of acoustic phonons, heating, nonthermal behavior of materials at or near the melting point, and phase transitions. Rentzepis and co-workers[45−47] and Larsson et al.[48] carried out X-ray diffraction studies of heat propagation in laser-shocked metallic or semiconductor crystals with a resolution of 10 ps, while reversible disordering in InSb and germanium was studied by Larsson et al.[49] and by von der Linde and Wilson and their co-workers.[50,51] Such studies were pursued, with a higher time resolution, by Cavalleri et al.[52] Coherent phonon propagation in GaAs was studied by means of subpicosecond X-ray diffraction by Rose-Petruck et al.[53] using a laser-generated plasma X-ray source (see section 5.1) and on InSb[54] using femtosecond X-ray pulses generated by Thomson scattering of a femtosecond laser pulse with the picosecond electron bunch from a linac. Coherent phonons were also observed in laser-excited InSb using a 100-ps-long X-ray pulse that is streaked after the sample (see section 5.3), thus achieving a resolution of <3 ps.[55,56] Coherent lattice vibrations of bismuth have also been probed with oscillation periods of ∼400 fs by von der Linde and co-workers[57] near the Lindemann stability limit, using 4.5 keV X-ray pulses from a laser-driven plasma source (see section 5.1). The Lindemann stability limit corresponds to bond distances, where the long-range order is lost and melting most likely occurs. Ultrafast solid−solid-phase transitions in VO_2 were studied by Cavalleri et al.[58] in relation to magnetic phenomena. Rousse and co-workers succeeded in obtaining femtosecond X-ray diffraction patterns of laser-induced disorder dynamics of organic solids, consisting of Langmuir−Blodgett multilayer films of cadmium arachidate.[59,60]

As far as theory is concerned, standard books on the theory of X-ray diffraction[61,62] describe in detail how X-rays scatter off atoms undergoing incoherent lattice vibrations. This gives rise to well-known effects such as Debye−Waller broadening, corresponding to a decrease in the intensity of the Bragg peak, or diffuse scattering, corresponding to an increase in the wings around the specular X-ray reflection. In any theoretical description of these effects, a time-average of the calculated diffraction intensities is carried out that is no longer valid when performing experiments on the time scale of vibrational periods. The approaches to calculate the angle-dependent diffracted intensity are based on two different theoretical approaches: the kinematical,[62] which is based on an extension of the treatment of scattering for incoherent vibrations to the time domain, and the dynamical diffraction theory,[43,56,63,64] which considers extinction effects of the incident X-ray beam in the solid. The latter was successfully applied to the case of coherent phonon oscillations of InSb.[56] Finally, Ma et al developed a theory of ultrafast time-resolved X-ray diffraction and applied it to the dissociation dynamics of finite systems.[65]

The examples cited above deal with solid materials (metals, semiconductors, or insulators), in which a bulk effect (e.g., coherent phonons, melting, etc.) is induced by the laser and subsequently probed with X-rays. Therefore, nearly all atoms in the interrogated volume participate to the scattering process. For chemical purposes, one needs structural information on the atomic-scale of time and space during the response of molecular entities to light. Few studies have dealt with chemical or biological systems, and while most of them dealt with bulk samples (e.g., organic solids or protein crystals), none of them concerns the subpicosecond time domain. Nanosecond time-resolved crystallography of myoglobin protein crystals and of a xanthopsin cycle was demonstrated using a 150 ps X-ray pulse from a synchrotron.[66,67] Structural changes in a photosensitive organic solid were resolved down to ∼100 ps, using the same setup.[68] However, some crucial issues need to be solved in order to reach a molecular level description of chemical processes by ultrafast techniques, which are related to the following facts:

(i) X-ray diffraction works best with ordered and/or highly concentrated samples.

(ii) In order to obtain a good scattered signal, the pump laser should excite as many species as possible. This often implies photochemical and/or laser-induced structural damage to the crystal, bearing in mind that the latter cannot be renewed easily during the experiment.

(iii) Damage by the X-ray pulses is an important and still unresolved issue.

(iv) Last, to obtain full structural information, a large number of Bragg reflections need to be monitored. Upon onset of disorder the spots in the diffractogram will experience a decrease in intensity. In most of the above-cited examples on the subnanosecond time scales, only one Bragg reflection was used at a time, which is not sufficient to retrieve a global structure. Two recent exceptions, however, demonstrate that this limitation may be overcome, at least for bulk samples: One is the powder diffraction study of the DMABN molecular crystal at a time resolution of 100 ps, where several Bragg reflections

were simultaneously recorded and geometries of different short-lived transients could be extracted.[68] The other is a sequence of six snapshots of the Laue pattern of photoexcited MbCO ranging from the subnanosecond to microsecond time scales, showing the movement of photodetached CO from the heme center.[69]

A solution to some of these issues would be to work in disordered media. As already mentioned, X-ray scattering of gases has been known since 1929,[44] and for liquids it was routinely used to determine the structure of the solvation shell around single ions (e.g., ref 70). To date, there has been, to our knowledge, only one pump−probe experiment based on X-ray scattering of the photodissociating I_2 molecule in liquid CH_2Cl_2 solvents, which was limited to the 100 ps time domain.[71] The scarcity of time-resolved X-ray scattering studies on gas- or liquid-phase samples stresses the difficulties of extending them to the ultrashort time domain, as the molecular signals are weak and are riding on the intense solvent-induced background diffraction pattern.

Disordered media have been dealt with more from a theoretical point of view. One of the first treatments of ultrafast time-resolved X-ray scattering was carried out by Wilson and co-workers, who used classical MD simulations to compute the diffraction pattern resulting from I_2 photodissociation in the gas phase and in solvents.[72] In addition, they have theoretically illustrated how the change in electron density upon electronic excitation of atoms can change their X-ray (and also electron) diffraction intensities.[41,42] The results indicate that electronic structures of excited electronic states may be directly observed using X-ray diffraction probe techniques and that inelastic scattering can be employed to measure the time dependence of electron correlation and nonadiabatic effects in curve-crossing events in molecules. More recently, Bratos and co-workers[73] modeled the above-mentioned results of Neutze et al on the diffuse scattering of I_2 in solutions,[71] using a theory where the electromagnetic fields are treated in the frame of Maxwellian electrodynamics, whereas the molecular system is treated quantum mechanically. One should, however, stress that diffuse scattering on kinetic time scales (ca. 100 ps and larger) will also include difference patterns between the excited and the dark sample merely due to solvent response. Indeed, a photochemical reaction generally releases heat into the bath, which can equilibrate on a picosecond time scale, depending on the concentration of the solute and the laser fluence used for excitation. This expected change has to be subtracted from the experimental data in order to be able to extract the desired solute response. So far, this complication has not been fully dealt with in experiments.

In summary, X-ray diffraction offers the following advantages:

(a) A *direct* connection between atomic positions and the scattering amplitude can be obtained via the Fourier relation.

(b) Visualization of electron densities, including global structures, is possible.

(c) All forms of samples can be investigated, in principle.

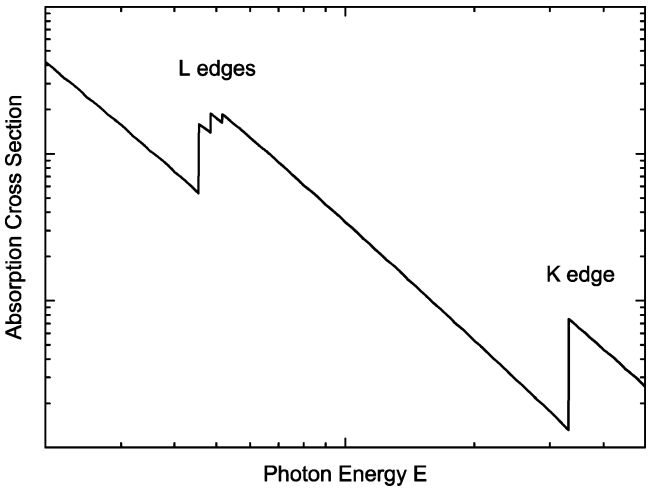

Figure 2. Variation of the linear X-ray absorption coefficient of an atom as a function of the photon energy.

(d) Spectroscopically dark species (intermediates) can be observed.

In practice, and regardless of the type of X-ray source (see section 5.1), the full implementation of ultrafast time-resolved diffraction still needs to overcome the problems related to issues i−iv, mentioned above.

Since most of natural and preparative chemistry and of biology take place in such liquid media, a technique that allows visualization of the structural dynamics of species in disordered media is highly needed. Time-resolved X-ray absorption offers such a possibility.

3. X-ray Absorption Spectroscopy (XAS)

X-ray absorption spectroscopy measures the absorption of X-rays as a function of incident X-ray energy E. In such a plot (Figure 2) the X-ray absorption coefficient shows three general features:[74]

(1) An overall decrease in X-ray absorption with increasing energy. This feature is illustrative of the well-known quantum-mechanical phenomenon of X-ray absorption by atoms.[75]

(2) The presence of saw-tooth-like features with a sharp rise at discrete energies, called absorption edges. The energy positions of these features are unique to a given absorbing atom. They occur near the ionization energy of inner shell electrons and contain spectral features due to core-to-unoccupied valence orbital transitions and core-to-continuum transitions.

(3) At energies above the edges, an oscillatory structure appears for molecules and solids that modulates the otherwise smooth absorption profile, typically by a few percent of the absorption edge jump. This feature, which is absent for single atoms in the gas phase, contains precise structural information such as interatomic distances and coordination numbers (see below).

Many excellent books and reviews exist that give a detailed description of XAS (e.g., refs 74, 76−80). Our aim here is to briefly review the basic principles behind the interpretation of the absorption features near the edge (the so-called XANES = X-ray absorp-

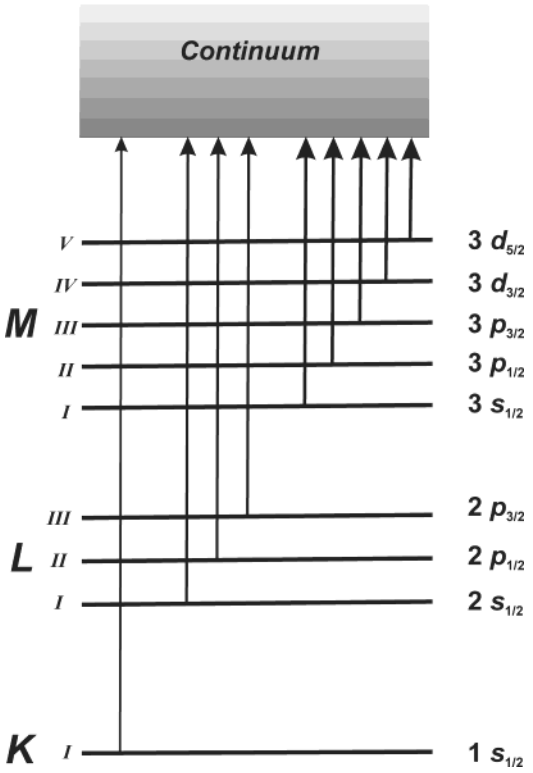

Figure 3. Transitions resulting from the absorption of X-rays. The transitions are accompanied by the production of a photoelectron.

tion near-edge structure) and above the edge (the EXAFS = extended X-ray absorption fine structure). Hereby we will treat all processes that occur in the energetic vicinity of the absorption edge as XANES, and this includes bound−bound and bound−continuum (e.g. shape resonance) transitions, as well as multiple scattering processes.

As mentioned above, the absorption edges are related to the transitions that excite a particular atomic core-orbital electron to the free continuum (ionization of core orbitals) or to unoccupied bound levels just below the ionization limit. The nomenclature for X-ray absorption features reflects the core orbital, from which the absorption originates (Figure 3). For example, K edges refer to transitions from the innermost $n = 1$ electron orbital, L edges refer to the $n = 2$ absorbing electrons (L_I to 2s, L_{II} to $2p_{1/2}$, and L_{III} to $2p_{3/2}$ orbitals), and M, N, etc., to the corresponding higher lying bound core shells. The transitions are always referred to unoccupied states, i.e., to states with a photoelectron above the Fermi energy (E_F), leaving behind a core hole, and absorption features may appear just below the edge, which correspond to transitions to bound unoccupied levels just below the ionization limit.

Above the ionization limit, the excited electron is often referred to as a photoelectron, and in a solid, depending on its kinetic energy, it can propagate more or less freely through the material. This occurs even in insulators, since the excited states are almost always delocalized states (quasifree states in molecules and conduction band states in solids).

Photoelectrons propagate through the solid as a spherical wave with a kinetic energy E_{kin} given by

$$E_{kin} = h\nu - E_B \tag{3}$$

where $h\nu$ is the incident X-ray energy and E_B the binding energy (which may be close to the Fermi energy). The photoelectron wave vector is then defined as

$$k = \frac{2\pi}{\hbar}\sqrt{2m(h\nu - E_B)} \tag{4}$$

When zooming into one of the absorption edge features in Figure 2, a fine structure can be seen; see Figure 4 for an example of the X-ray absorption spectrum of $K_4[Fe(CN)_6]$, in the region around the Fe K edge. This region is usually divided into two parts: The low-energy part just below, at, and just above the edge is due to XANES according to our definition given above, while the part at energies significantly (tens to hundreds of electronvolts) above the edge is due to EXAFS, which shows an oscillatory structure. We now discuss the information content of these two regions of the XAS spectrum.

3.1. Extended X-ray Absorption Fine Structure (EXAFS)

The EXAFS region covers the high-energy continuum above the ionization threshold (this lies at ~7.14 keV for the K shell of Fe^{II}; Figure 4). In this regime, the photoelectron states approximate spherical waves. The oscillatory structure is due to the interference between the outgoing photoelectron wave and the wave scattered back at neighboring atoms, as depicted in Figure 5. It therefore does not exist in the case of the isolated atom. At high photoelectron kinetic energies, the scattering of electrons is such that the only significant contributions to the final state wave function in the vicinity of the absorbing atom comes from paths in which the electron is scattered only once (single scattering events, Figure 5).[81] The photoelectrons emitted from the excited atom as spherical waves damp out rapidly due to inelastic effects caused by the extended valence orbitals of the nearby-lying atoms. This limits the probed spatial region and ensures that multiple-scattering effects beyond simple backscattering can be ignored. The fact that multiple-scattering events can be neglected allows the analysis of the data by a simple Fourier transformation.[82] For this purpose one has to generate a normalized X-ray absorption spectrum (normalized to the absorption edge jump under consideration), which is defined as the normalized oscillatory part of $\mu(E)$ (the X-ray absorption coefficient), i.e., the EXAFS, via

$$\chi(E) = \frac{[\mu(E) - \mu_0(E)]}{\Delta\mu_0(E)} \tag{5}$$

with $\mu_0(E)$ being the smoothly varying atomic-like background absorption and $\Delta\mu_0$ a normalization factor that arises from the net increase in the total atomic background (or simply the absorption edge jump). Above the edge under consideration, using eq 4 to substitute E with the photoelectron wave vector, we can rewrite $\chi(k)$ as

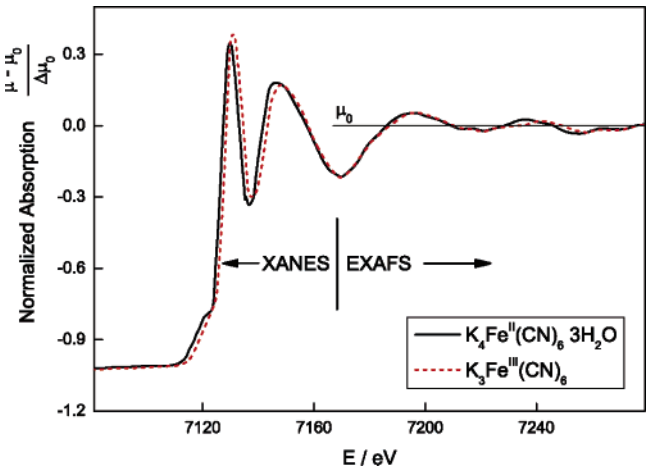

Figure 4. K edge X-ray absorption spectra of iron in $K_4Fe^{II}(CN)_6$ and $K_3Fe^{III}(CN)_6$ bulk samples. The relative absorption with respect to the high energy background is plotted. Reprinted with permission from ref 99. Copyright 1988 Wiley.

$$\chi(k) = \sum_j S_0^2 N_j \frac{|f_j(k)|}{kR_j^2} \sin[2kR_j + 2\delta_e + \Phi] \exp(-2R_j/\lambda(k)) \exp(-2\sigma_j^2 k^2) \quad (6)$$

which is the standard EXAFS formula. The structural parameters (for which the subscript j refers to the group of N_j atoms with identical properties, e.g., bond distance and chemical species) are (a) the interatomic distances R_j, (b) the coordination number (or number of equivalent scatterers) N_j, and (c) the temperature-dependent root mean square fluctuations in bond length σ_j, which should also include effects due to structural disorder.

In addition, $f_j(k) = |f_j(k)| \exp(i\phi(k))$ is the backscattering amplitude, δ_e is the central-atom partial-wave phase shift of the final state, $\lambda(k)$ is the energy-dependent photoelectron mean free path (not to be confused with its de Broglie wavelength), and S_0^2 is the overall amplitude reduction factor. Moreover, although the original EXAFS formula referred only to single-scattering contributions from neighboring shells of atoms, the same formula can be generalized to represent the contribution from N_R equivalent multiple-scattering contributions of total path length $2R$.[74]

In a very transparent and simple form, eq 6 contains all of the key elements that provide a convenient parametrization for fitting the local atomic structure around the absorbing atom to the measured EXAFS data. The dependence of the oscillatory structure on interatomic distance and energy is clearly reflected by the $\sin(2kR)$ term. The decay of the wave due to the mean free path or finite lifetime (including the ultrashort core-hole lifetime) of the photoelectron is captured by the exponential term $\exp(-2R/\lambda)$. This factor is largely responsible for the relatively short range (generally a few tens of angstroms) in a material probed in an EXAFS experiment. The strength of the reflected interfering waves depends on the type and number of neighboring atoms and is given by the backscattering amplitude $|f_j(k)|$ and hence is primarily responsible for the intensity of the EXAFS signal. Other factors, namely, the spherical-wave factors $(1/kR^2)$ and mean-free-path terms, appear secondary but are important for a quantitative description of the EXAFS amplitude. The phase factor $\Phi = \arg f(k)$ reflects the quantum-mechanical wavelike nature of the backscattering process. A somewhat larger contribution to the overall phase is given by the phase shift $2\delta_c$ at the position of the absorbing atom, since the photoelectron encounters the potential created by this atom twice. These phase shifts account for the difference between the measured and geometrical interatomic distances, which is typically a few tenths of an angstrom and must be corrected by either a theoretical or an experimental reference standard. The $\exp(-2\sigma^2k^2)$ term, representing the Debye−Waller broadening to a good approximation, is partly due to thermal effects, which cause the atoms to jiggle around their equilibrium atomic positions. These slight movements smear out the otherwise sharp interference pattern of the rapidly varying $\sin(2kR)$ term with increasing k. The effects of structural disorder are similar and they give an additive contribution to σ^2. The Debye−Waller effect seems more pronounced at shorter photoelectron wavelengths, and hence it terminates the EXAFS at sufficiently large energy beyond $k \sim 1/\sigma$, which is typically around 10 $Å^{-1}$. Finally, S_0^2 is a many-body effect due to the relaxation of the system in response to the creation of the core hole. It is usually approximated by a constant. Using eq 6, it can be seen that a Fourier transform of the EXAFS with respect to k corresponds to an effective radial distribution function, with peaks near the first few nearest neighbor distances, provided the phase shifts are correctly dealt with. Other improvements to the theory have been amended, such as multiple scattering and curved-wave effects,[74] but for the purpose of this review, eq 6 accurately describes the connection between the measured EXAFS and the local geometric structure that causes it.

3.2. X-ray Absorption Near-Edge Structure (XANES)

The region around the absorption edge up to ca. 20−50 eV above the edge (Figure 4) corresponds to the XANES. Different than EXAFS, which is mainly a structural technique, XANES contains information about both the electronic and the molecular structure. Indeed, it has been shown that XANES is in part determined by the geometrical arrangements of the atoms in a local cluster around the X-ray absorbing atom in biological systems,[83] surfaces,[84] solids, and solutions.[85] This comes about via multiple scattering of the excited photoelectron, as shown in Figure 5b, and is different than EXAFS, which is dominated by single scattering events.

Furthermore, the absorption features in the 10 eV energy range above the absorption threshold (which often is just below the ionization threshold of a given shell) have a physical origin, which is different for different classes of materials: bound valence states or quasibound states (so-called shape resonances in molecules), core excitons in ionic crystals, unoccupied local electronic states in metals and insulators, etc. Thus, the region of the edge that lies below the

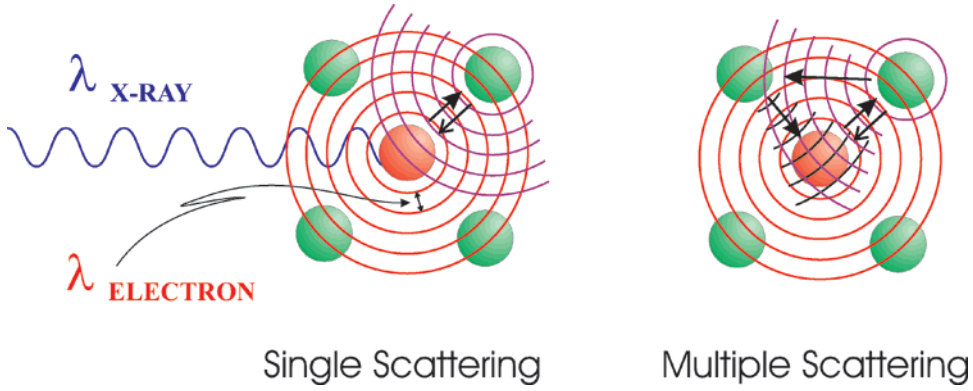

Figure 5. Pattern of an outgoing and backscattered photoelectron wave in the case of EXAFS (single scattering events) and XANES (multiple scattering events).

ionization threshold is dominated by such excitations, while the region above the ionization limit is governed by multiple scattering events. Much valuable electronic and structural information, which we now discuss, can be unraveled by a careful analysis of the XANES regions.[86]

3.2.1. Identifying the Low-Lying Excited States of Molecules

These are the states that bind the systems together in molecules and solids and determine their electronic structure. The states populated by the excited electrons in XANES belong to this category. They encompass all the unoccupied states from the Fermi level up to the ionization limit. Thus, in transition metals, the XANES features include the unoccupied states of the narrow d bands, just above the Fermi level, and the less tightly bound s and p bands in solids. For molecules or complex ions, the XANES states include unoccupied bound states as well as the low-lying continuum. Thus, a theoretical analysis of XANES implies solving the Schrödinger equation for a range of energies at the lower end of which the interaction of the electrons with the atom is very strong, becoming weaker with increasing energy. In addition, since the XANES transitions are subject to the same selection rules as optical ones, and since these rules can be relaxed by the local symmetry around the absorbing atom,[87] information about the local geometrical arrangement can be obtained, for example, when forbidden transitions show up in XANES spectra.

3.2.2. Valence and Chemical Shift of Atoms

The effective atomic charge of an atom in a molecule or a crystal can be measured by the "valence shift" of the core level binding energy observed by X-ray photoelectron spectroscopy (XPS) or ESCA. This is done by comparing the spectra of two compounds with different oxidation states, e.g., Fe^{II} and Fe^{III} of iron hexacyanoferrate, whose XAS are shown in Figure 4. Because of the overlap of bound excited states with the ionization threshold and with multiple-scattering resonances in the low-energy continuum, it is not always straightforward to measure binding energies in the XANES region. This is further complicated by the fact that the absorption fine structure of a specific element is strongly influenced by the nature of its ligands (e.g. because of the degree of covalence in the bonding), giving rise to the so-called "chemical shift". Notwithstanding these complications, for many molecular and condensed phase systems, a linear relationship has been established between the energy of the first peak (or peaks) in XANES and the binding energy obtained from XPS.[77] Alternatively, a linear dependence of the energy position of the first XANES lines with the oxidation state of the atom has been demonstrated and proposed as a means to determine the latter.[88−91] With laser−X-ray pump−probe techniques it is now possible to measure valence shifts with high precision (see section 6.3).

3.2.3. Multiple Scattering

As mentioned above, multiple scattering resonances in XANES of molecules and condensed materials cause modulations of the atomic X-ray absorption cross section of the absorbing atom. In highly symmetric molecules (e.g., SF_6, CF_4, SiF_4, $SiCl_4$, etc.), strong resonances (similar to the so-called shape resonances in electron−molecule scattering) appear in the continuum region above the ionization threshold. They are due to the multiple scattering and interference of the photoelectron, stemming from the central atom, with the symmetrically surrounding atoms. The scattering effect can be considered as a quasipotential superimposed on the Coulomb potential of the central atom, which temporarily traps photoelectrons released by X-ray excitation of the central atom. XANES features in molecules are therefore very sensitive to small changes of the molecular geometry and can even couple with nuclear motion.[92−96] The shape of XANES spectra—concerning the number of multiple-scattering resonances and their relative intensities—is similar for each type of molecular symmetry. Thus, the geometry of a molecule can easily be recognized by the shape of its XANES spectrum, and the energy positions of the multiple scattering resonance peaks are strongly dependent on interatomic distance.[97,98] Furthermore, the spectra of K edges are very different from those of $L_{II,III}$ edges since K shells release p-electrons and L_{II} and L_{III} shells release s and/or d electrons.

In the language of scattering theory, one can say that at high energies the scattering of excited electrons is weak, such that the only significant contri-

butions to the final state wave function in the vicinity of the absorbing atom come from paths in which the electron is scattered only once (EXAFS). However, when lowering the photoelectron energy into the XANES region, multiple scattering becomes more and more dominant. It appears from the above that because multiple scattering is sensitive to multiatom correlations, it delivers information not only on the radial distances of the surrounding atoms but also on their orientations relative to one another, including bond angles. In comparison, EXAFS only delivers the pair correlation function and the mean displacement.

In summary, direct structural information can be extracted from XANES, which, like EXAFS, is due to scattering of the photoexcited electron by neighboring atoms. However, while for EXAFS the theory is straightforward and easy to handle, XANES requires more elaborate theories beyond one-electron theories.[99,100] Furthermore, electronic interactions complicate matters and their theoretical treatment is specific for each class of atom and requires introducing spin−orbit effects, crystal-field effects, and multiplet effects that originate from two-electron Coulomb and exchange interaction between electrons from different orbitals.[80,101] This, combined with the overlapping contributions that occur in the XANES, have delayed its use as a structural technique compared to EXAFS. However, it is commonly used as a technique to investigate the electronic structure of various materials.[100,102]

3.3. X-ray Fluorescence Excitation Spectroscopy

X-ray absorption spectroscopy deals with the attenuation of the sample transmission. A variant of this method is to record excitation spectra of the subsequent fluorescence, which mainly stems from the next higher lying shells. For X-ray fluorescence, the transitions are classified as shown in Figure 6. In this picture, a K-shell excitation induces emissions from the $n \geq 2$ shells to $n = 1$, as well as subsequent emissions from $n \geq 3$ shells to $n = 2$, which occur in a cascade. An L-shell excitation can only induce transitions from $n \geq 3$ shells, and from $n \geq 4$ to $n = 3$, and so on. Actually, the situation is a little more complicated than depicted in Figure 6, where the orbital and spin components of the levels are not shown.

Analogous to the case of optical spectroscopy of valence electrons, if one collects the global fluorescence intensity as a function of incident photon energy, the excitation spectrum should be a mirror image of the transmission spectrum (provided the quantum yield of global fluorescence is not energy-dependent). In principle, one can achieve excitation spectra with zero background, if one chooses the right edges, i.e., in general the lowest spin−orbit component of a principal series. If dispersed fluorescence (monochromatized fluorescence) is detected, then the excitation spectrum may still reflect the absorption profile, if all absorbing states permit the same level to emit with a constant quantum efficiency. If this is not the case, then the excitation spectrum will

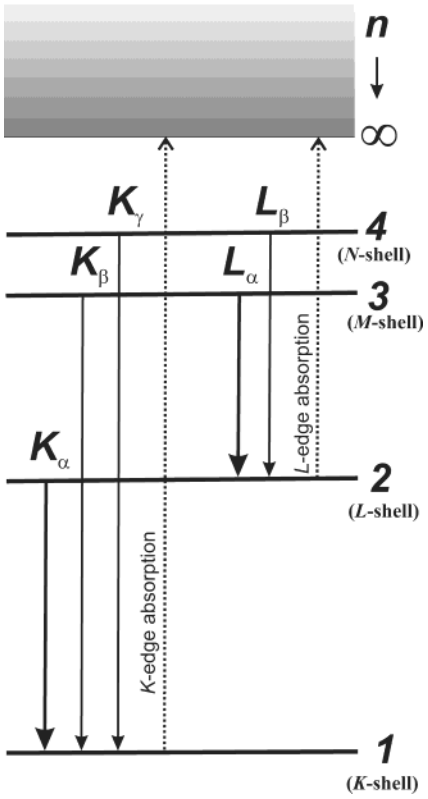

Figure 6. X-ray emission lines (solid arrows) following the ejection (dashed arrows) of an electron from the K and L shell.

contain information about the relaxation pathways, i.e., which absorbing state populates a given (selected) emitting level.

In X-ray spectroscopy, there exists an additional advantage for using fluorescence rather than transmission, which is related to the issue of lifetime broadening. Indeed, XANES features are often smeared out because of the natural line width that arises from the finite lifetimes of the core holes. The energy width increases with atomic number Z, and for K shells it spans from 0.86 eV (for $Z = 21$) up to 40 eV (for $Z = 74$).[103] To overcome this limitation, Hämäläinen et al.[104] proposed to use a highly monochromatic incident X-ray beam whose energy is scanned across the absorption edge, while the characteristic fluorescence is monitored with a resolution superior to that of the natural line width. Different improvements of this technique have since then been proposed.[80,105]

To summarize, XAS offers the following advantages:

(i) it can be implemented in any type of media: gases, liquids, and solids (amorphous or ordered).

(ii) It is highly selective, since one can interrogate one type of atom specifically, e.g., the central atom of a given solute inside a bath of solvent species by simply tuning into its characteristic absorption edge.

(iii) It probes mainly the local structure around the atom of interest, which is fine for ultrafast processes, since short time scales correspond to short distance scales, i.e., on the femtosecond time scale the evolving chemical reaction affects only nearest neighboring atoms.

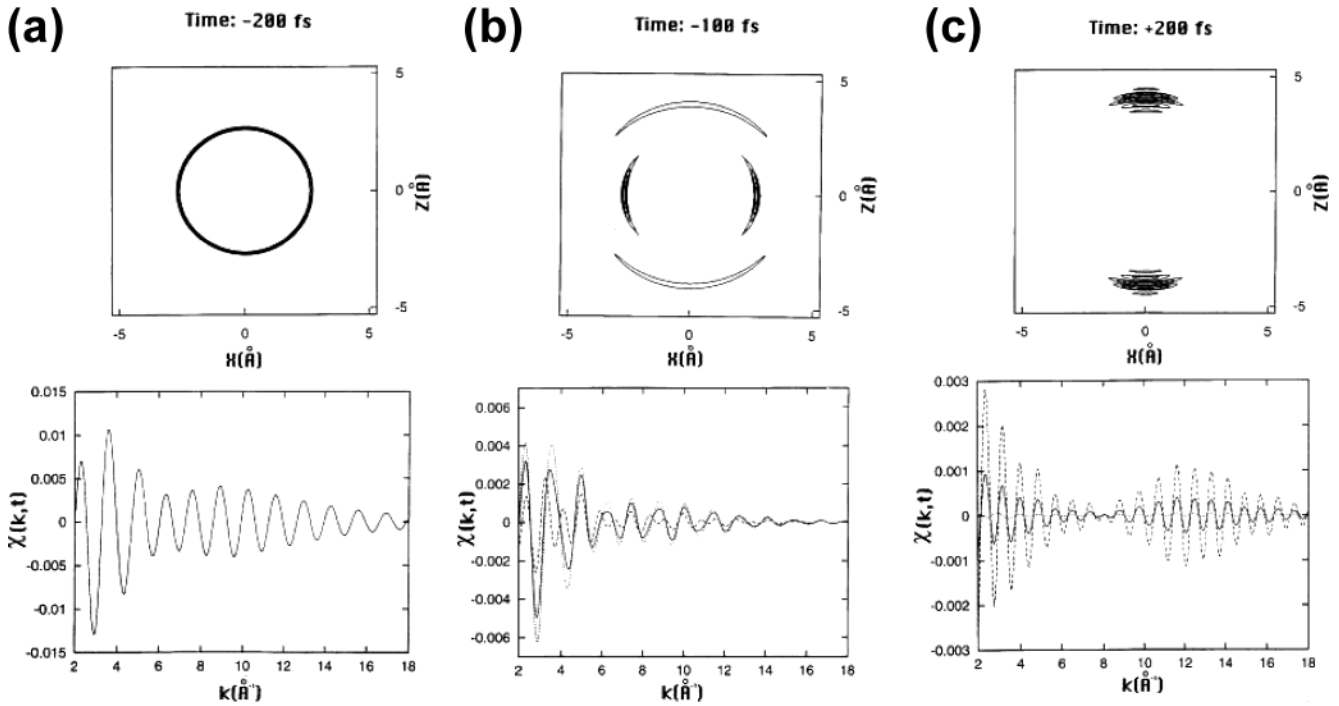

Figure 7. Top panels: Contour plots (arbitrary units) of the internuclear separation (in Å) shown as a probability distribution function in the $x-z$ plane for I_2, 200 fs (a) and 100 fs (b) prior to and 200 fs (c) after perturbation by the laser pump pulse. At −200 fs, zero probability is excited to the B excited state of I_2 (in ref 106, a π-pulse was used, which allows full inversion of the population between the ground and the excited state). Since the initial distribution is spherically symmetric, rotation about the y-axis gives an identical distribution. At −100 fs, partial excitation of the B-state has occurred, while at 200 fs the excitation is nearly complete. Bottom panels: The EXAFS at −200 fs corresponds to the radial distribution of the top panel. z-polarized, and x-polarized EXAFS results are identical due to the symmetry of this configuration. At −100 fs, the three spectra correspond to X-ray polarization averaged (solid line), z-polarized (dashed), and x-polarized (dotted line) EXAFS measurements. Since the z-polarization of the pump pulse **E**-field defines an axis of symmetry, any X-ray polarization within the $x-y$ plane will give the same results as the dotted line. Note that the scaling with respect to the −200 fs case has changed. For 200 fs, there is a large discrepancy between the (strong) z-polarized and the (weak) x-polarized EXAFS. This effect is a clear indication that the I_2 molecule has oriented itself predominantly along the z-axis. Reprinted with permission from ref 106. Copyright 1999 American Institute of Physics.

(iv) It delivers both electronic and structural information. This is essential in chemistry, as it is the electronic structure changes that drive the nuclear dynamics (at least in a Born−Oppenheimer regime).

(v) The precision of structural determination by EXAFS is on the order of $10^{-2}-10^{-3}$ Å, which is very good for observing the transient structures of reaction intermediates.

(vi) Using polarized X-ray pulses and laser-aligned samples permits the measurement of orientation-dependent spectra.

These advantages are particularly attractive for the study of dynamical processes in chemistry, biology, and material science and call for the extension of XAS to the ultrashort time domain.

4. Time-Resolved X-ray Absorption

Extending XAS to the time domain implies the demonstration of its conceptual and practical feasibility. In this section, we review some of the work that has dealt with these questions. These concern the demonstration that (a) time-resolved EXAFS does deliver structural information about transient molecular structures and (b) the type of signals one anticipates with present day and future sources of ultrashort X-ray pulses can deliver the desired structural information.

4.1. Theoretical Considerations

The theoretical studies we review here help make some predictions about the type of results one would anticipate from time-resolved XAS experiments[106] but did not address the actual feasibility of these experiments.

First, it should be mentioned that in XAS, the processes of ejection, backscattering, and interference are extremely fast. For inner shell electrons with ionization energies above 1 keV, these processes are mostly completed well within ∼1 fs, as can be seen from the measured homogeneous line widths of the absorption edges.[103] This means that XANES and EXAFS take a truly instantaneous snapshot of immobile atoms, even during a violent chemical reaction. Therefore, implementing ultrafast time-resolved XAS via the pump−probe scheme (Figure 1) is straightforward.

Brown et al.[106] verified this conjecture in a rigorous theoretical description of time-resolved EXAFS in the case of excited-state dynamics of the I_2 molecule in the gas phase. They developed a formalism to extend the usual EXAFS function (eq 6) to the time domain that takes into account the creation of a vibrational wave packet in the excited molecule and the finite duration of the X-ray probe pulse. They applied their formalism to the case of the excitation of I_2 to its

covalent B $^3\Pi_0$ state, using different polarizations of optical pump and X-ray probe pulses.

Figure 7 shows snapshots of the internuclear separation (upper portion) in angstroms and of the-EXAFS signal (lower portion) at three different times: −200 fs (a) and −100 fs (b) prior to excitation and 200 fs (c) after excitation by a 100 fs optical pulse. The figure for $t = -200$ fs, reflects the fact that the nuclear probability distribution of the ensemble of ground-state I_2 molecules is isotropic in space with a mean radius corresponding to the equilibrium bond length of I_2 (2.67 Å) and a very narrow radial spread due to the zero point motion along the internuclear coordinate. The spherically symmetric nature of the probability distribution ensures that any X-ray polarization will provide an equivalent result. Upon excitation with the pump−pulse polarized along the *z*-direction, the average bond length of the photoexcited I_2 increases, when it accesses the B state. Already at −100 fs the effect of the 100 fs pump−pulse (or its leading tail) is evident. Since EXAFS measures the backscattering of photoelectrons off neighbors, the EXAFS signal decreases (compare with the figure at $\Delta t = -200$ fs). This is because the X-ray polarization only allows those molecules to be excited , that are aligned in the *z*-direction (those in the B state), while the remaining ground-state molecules are not subject to X-ray absorption. A minor effect for the overall amplitude reduction of the EXAFS signal lies in the decreased backscattering amplitude (the $1/R^2$ term in eq 6), which accounts for the fact that the nearest neighbor distance increases. The signal also oscillates at a somewhat higher frequency in *k*-space. This effect comes from the sin term in eq 6 and was already mentioned in section 3.1.

Brown et al.'s time-dependent, quantum-mechanical calculations also demonstrate that the spread of the wave packet makes the extraction of radial distribution functions problematic. The diffuse nature of the nuclear probability distribution is not amenable to the description by a time-dependent Debye−Waller factor. Rather, extraction of structural information will better be carried out based on classical or semiclassical molecular dynamics simulations, where wave packet spreading is lessened, or by iterative fitting of experimental spectra to model spectra based upon parametrized functional forms for nuclear distributions.

Coming back to the experimental issues, the simulations of Brown et al. demonstrated the conceptual feasibility of ultrafast EXAFS. Their conclusions should also, in principle, be valid for time-resolved XANES. The actual experimental implementation of ultrafast time-resolved XAS requires a number of conditions to be fulfilled, which we now discuss.

4.2. Experimental Considerations

When extending the pump−probe scheme (Figure 1) into the X-ray domain, we deal with two very different pump and probe light sources with respect to their pulse intensities. This poses stringent boundary conditions on the sample design in order to guarantee a feasible experiment. This section deals with model calculations, which include these constraints, but also prepare the ground, when new sources will become available (see section 7). These calculations will be illustrated on practical examples concerning transition-metal compounds. The considerations developed here have already been discussed in part by the authors.[107−111]

To start with, we need to estimate the signal-to-noise ratio that one can anticipate with state-of-the-art technology. Hereby, we will restrict the model calculations to pump−probe experiments in transmission mode. X-ray fluorescence excitation spectroscopy (see section 3.3) is the method of choice when dealing with very dilute samples (e.g., with concentrations <1 mmol/L; see also section 6 for examples of experimental results in transmission mode), but for larger concentrations in the 10−100 mmol/L range, probing in transmission mode provides generally superior signal-to-noise ratios.

While most ultrafast XAS studies nowadays exploit 30−100 ps long X-ray pulses from a synchrotron (see section 6), they already provide us with much insight into the details of a desired setup exploiting future femtosecond hard X-ray sources. Since the goal here is to lay the grounds toward ultrafast temporal resolution, we will consider femtosecond laser systems as the excitation source, although the currently larger synchrotron radiation pulse widths would also warrant the use of picosecond lasers. Commercial femtosecond lasers are nowadays limited to 1−5 W of average output power, which is roughly constant for all pulse repetition rates. For example, for a 1 kHz repetition rate the pulse energy at 800 nm lies between 0.5 and 3 mJ, which translates to about $10^{15}-10^{16}$ laser photons per pulse available for sample excitation. The weakest link is therefore given by the rather low X-ray pulse intensity, which typically contains 10^3-10^6 photons per pulse (and 0.1% bandwidth) at different third-generation synchrotron radiation beamlines.

In an experiment one would typically seek to accumulate pump−probe shots for up to 1−10 s per data point, so that an entire energy scan at a given pump−probe time delay would take on the order of 10−30 min. If we consider ca. 10^4 photons/pulse/0.1% bandwidth as a starting value for the X-ray pulse intensity, then we demand in return to observe the photoinduced XAS change after accumulating ca. 10^7-10^8 incident X-ray photons per data point. This boundary condition necessitates the optimization of the sample in order to minimize the number of X-ray photons required to measure a given X-ray absorption cross section with the highest possible accuracy (thus maximizing the signal-to-noise ratio S/N).

Before going into the details of the sample optimization, it is helpful to sketch out the basics behind these considerations. If we neglect the photoexcitation process for the moment (i.e., assuming always 100% excitation of the sample), in general, increasing the solute concentration *c* and decreasing the sample thickness *d* optimizes the conditions for measuring time-resolved XAS, until we decrease the solute-only transmission to ca. 10.85% (or ca. 0.96 OD) (see below). Thus, we can determine the optimum concentration of a given solute, if we fix the sample thickness *d*. Typical thicknesses for liquid jets or liquid-containing cuvettes range from ca. 0.1 mm to

several millimeters. Thinner jets are possible but not necessarily useful, since the optimum concentration would be too large, e.g., exceed the solubility limit of the solute. Too large thicknesses, on the other hand, would suffer an overall decrease of S/N, due to the increasing background absorption.

Regardless of the choice of the sample thickness, we will show below that the *total* amount of sample particles in the X-ray probe beam under optimized conditions is directly proportional to the X-ray spot size and inversely proportional to the X-ray absorption cross section, whose photoinduced (small) changes we want to measure. Typical X-ray foci at synchrotrons are in the 0.1−0.3 mm range. For typical examples, as will be treated below, this means that we have between 10^{14} and 10^{16} molecules in the probed volume. To achieve a reasonable photoinduced signal, we should excite as many solute molecules as possible. Neglecting the optical absorption cross section for photoexcitation for the moment, this requires on the order of 10^{15} laser photons per pulse, or ca. 0.25 mJ of pulse energy (e.g., at 800 nm). In other words, one should aim to increase the laser pulse intensity, until full excitation is achieved, while remaining below pump intensities, which begin to stimulate effects (e.g. nonlinear absorption) that do not belong to the investigated process. As long as we are in the linear regime of the pump process, it is always preferable to increase the laser pulse intensity and sacrifice the repetition rate of the laser system. For the aforementioned laser systems, this argument motivates the use of a 1 kHz femtosecond laser rather than a multi-MHz system, which has orders of magnitude less energy per pulse. However, this results from the fact that we have to excite an extended volume of a given sample due to the given X-ray spot size. For example, assuming a microfocusing beamline with 10 μm spot size would reduce the number of probed solute species to below 10^{13} (or 0.6 μJ at 800 nm), and therefore, laser systems with much higher repetition rates and less energy per pulse may be considered to optimize the signal-to-noise ratio S/N of the experiment.

The above-mentioned estimates already sketch out the basic requirements for designing the sample and choosing the femtosecond laser for a given X-ray source. We will now treat this optimization process in great detail and illustrate it on our recent picosecond-resolved XAS experiments in section 6.3. We will start by describing the X-ray probe process and then treat the laser excitation process by assuming ideal linear absorption conditions.

4.2.1. The X-ray Probe Process

In the pump−probe experiments, we can describe the transmitted X-ray intensity as a function of the amount of excited species, thus modifying the Lambert−Beer law with respect to the photoexcitation yield $f(n_{sam})$, where n_{sam} is the sample concentration (in units of particles/mm^3). In the following analysis, we use a fixed sample thickness d = const. The main adjustable parameter is n_{sam}, which in turn affects the amount of excited-state species, $f(n_{sam})n_{sam}$, in the laser-illuminated volume, averaged over d. Below, we will estimate the photolysis yield $f(n_{sam})$ as a function of sample concentration using the linear Lambert−Beer law, taking into account the number of incident laser photons per pulse, $N^{ph}{}_0$, and the optical absorption cross section, σ_{opt}.

Since the X-ray probing process is linear due to the extremely low X-ray pulse intensities available today, we can calculate the probe signal with high accuracy. The Lambert−Beer law of the transmitted X-ray intensity can be written as a function of the fraction of excited-state species $f(n_{sam})$ (with $f = 0$ for the stationary sample) via

$$I_1 = I_0 \exp(-n_{sol}\sigma_{sol}d) \exp(-n_{sam}\sigma_{rest}d) \exp(-(1-f)n_{sam}\sigma_{gr}d) \exp(-fn_{sam}\sigma_{ex}d) \quad (7)$$

where n_{sol} is the solvent concentration; n_{sam} is the sample concentration; σ_{sol} is the X-ray absorption cross section of a solvent molecule; σ_{gr} is the X-ray absorption cross section of the unpumped selected atom at X-ray energy E_x; σ_{ex} is the X-ray absorption cross section of the excited selected atom (at E_x); σ_{rest} is the X-ray absorption cross section of all other particles, which build up the selected sample molecule (including e.g. counterions); $f = f(n_{sam}, N^{ph}{}_0, \sigma_{opt})$ is the photoexcitation yield of the sample particle; $I_0 = N^x{}_0\Phi_{det}$ is incident X-ray flux corrected for the quantum yield Φ_{det} of the detector; and $N^x{}_0$ is the number of incident X-ray photons on the sample per pulse.

Setting $\Delta\sigma_{ex} = \sigma_{ex} - \sigma_{gr}$, we can rewrite eq 7 as

$$I_1 = I_0 \exp(-n_{sol}\sigma_{sol}d) \exp(-n_{sam}(\sigma_{gr} + \sigma_{rest})d) \exp(-fn_{sam}\Delta\sigma_{ex}d) \quad (8)$$

Equation 8 then describes the transmitted X-ray intensity, I_1, as a function of the optical pump process. The third term, containing the photolysis yield f, defines the contribution of the excited-state species to the total transmitted intensity, thus the pump−probe signal. We can define the signal in this pump−probe process as the natural logarithm of the ratio of transmitted intensities between the laser-pumped ($I_1{}^{pum}$) and unpumped ($I_1{}^{unp}$) sample, which yields with eq 8

$$S = \ln\left(\frac{I_1{}^{unp}}{I_1{}^{pum}}\right) = fn_{sam}\Delta\sigma_{ex}d \quad (9)$$

(Using the base 10 logarithm instead of the natural logarithm would yield the definition for the change in optical density (ΔOD) due to photoexcitation, which is commonly employed in optical pump−probe measurements.) The sign of $\Delta\sigma_{ex}$ in eq 9 describes a transient absorption or bleach, which is proportional to the amount of excited-state species fn_{sam}.

In the experiment, the transmission intensities for the excited and the dark sample are determined by the number of X-ray photons recorded on the detector behind the sample, and we typically accumulate for several pump−probe shots, provided all electronic noise is suppressed. This leaves us with only the shot noise distribution, which is given by Poisson statistics of the transmitted pulse intensity. Indeed, we have recently demonstrated that we can suppress the

majority of electronic noise in an experiment, which validates this rather idealistic treatment.[110,111] Applying the error propagation formula to eq 9 then yields for the pump−probe signal S a shot-noise determined contribution N of

$$N = \sqrt{\frac{1}{I_1^{\text{pum}}} + \frac{1}{I_1^{\text{unp}}}} \tag{10}$$

The ratio between eqs 9 and 10 finally defines the signal-to-noise ratio S/N, which one seeks to maximize in the experiment. Mathematically, we find the optimum experimental conditions, e.g., the optimum sample concentration for a fixed sample thickness d, by finding the extreme value in

$$\frac{d}{dn_{\text{sam}}} S/N = 0 \tag{11}$$

If we assume that we can always excite the entire sample (thus $f = 1$), then eq 11 yields a concentration of n_{sam} for which the transmission through the sample only (thus neglecting the solvent) is 10.89% (or 0.96 OD). For example, in a stationary XAS experiment seeking to measure the EXAFS of a given molecule with the highest precision and using the least amount of X-ray photons possible, we would choose a concentration for which the transmission above the selected X-ray absorption edge of the entire molecule is exactly 10.89%. That is, this value includes the transmission through all atoms that make up the molecule (and for ionic samples also the counterions). Including the solvent contribution will always decrease the total transmission below this value, but this only reduces the overall S/N ratio, and not the optimum sample concentration, as derived from eq 11.

On the other hand, the photolysis yield depends on many parameters, including the number of laser photons for the excitation process itself. For example, if the laser has less photons per pulse than particles in the probed volume of the sample under the above-mentioned conditions, then the optimum concentration will be somewhat smaller. This requires a more careful consideration, and below we will estimate the ideal conditions assuming a linear excitation process.

4.2.2. The Laser Excitation Process

We now consider the photolysis yield $f(n_{\text{sam}},N^{\text{ph}}{}_0,\sigma_{\text{opt}})$. For one-photon absorption processes, we calculate the fraction f of sample particles that have been excited by the pump source, *averaged* over the constant thickness d of the sample, via the ratio of absorbed laser photons after the sample thickness d and the absolute number of sample particles in the illuminated volume Fd. We obtain

$$f(n_{\text{sam}},N^{\text{ph}}{}_0,\sigma_{\text{opt}}) = \frac{N^{\text{ph}}{}_0}{n_{\text{sam}}Fd}(1 - \exp(-n_{\text{sam}}\sigma_{\text{opt}}d) \tag{12}$$

where $N^{\text{ph}}{}_0$ is the number of incident laser photons per pulse, d is the sample thickness, F is the focal area illuminated by the laser, and σ_{opt} is the optical absorption cross section of the sample particle.

Ideally, F should have the size of the X-ray probe focus, and typical foci diameters are in the 100−300 μm range. In a typical experiment, a liquid jet is used, and $d = 0.1$ mm is therefore a typical value. Equation 12 is only valid when neglecting solvent and excited-state absorptions in the optical domain.

Applying $f = 1$ (thus complete photoexcitation) in eq 8, we already calculated the best sample concentration via eq 11 and thus quantified the best possible signal-to-noise ratio (S/N) under realistic probe conditions (e.g., the X-ray photon flux). This strongly aids in selecting possible experiments and allows us to assess the potential for success of a proposed EXAFS structural dynamics experiment under such pump and probe conditions. We choose EXAFS here, rather than XANES, because any result valid for time-resolved EXAFS guarantees the success of a time-resolved XANES experiment, due to its typically larger signal. The photoexcitation term in eq 8 contains the product of f and $\Delta\sigma_{\text{ex}}$, which governs the S/N ratio. While the validity of eq 12 is based on a strictly linear excitation process, it will generally deliver high-intensity pump conditions, which may in return enter the realm of nonlinear absorption processes in both the sample and the solvent. As a consequence, the photoexcitation yield may become considerably smaller than calculated via eq 12. Therefore, it is necessary to determine the amount of excited-state species in a separate optical measurement, and these results can be used in eqs 8−12 to calculate the feasibility of a given time-resolved EXAFS experiment.

4.3. Numerical Examples: The Case of Transition-Metal Compounds

As an illustration to the above discussion, we will consider the case of transition-metal complexes. Indeed, these are interesting in photochemistry and in biology, as they appear as photoactive chromophores in many systems.

Static EXAFS oscillations represent typically 1−20% modulation of the edge height (see, for example, Figure 4). Therefore, in the following we seek to measure the EXAFS with a noise level of $\chi = 1\%$ relative to the absorption edge jump of the selected transition metal. We will further assume a reasonable value of $f = 10\%$ for the amount of excited-state species, and we will calculate the required number of incident X-ray photons to measure the EXAFS with $S/N = 1$ (for 1% changes relative to the edge jump). The results will then deliver a reasonable estimate for the feasibility of such an experiment. Note that the number of required X-ray photons for such an experiment scales with

$$I_0 \propto \left[\frac{S/N}{f\chi}\right]^2 \tag{13}$$

which means that we can adjust our results for experimentally derived f values, as well as demand a larger S/N or be able to measure a smaller EXAFS χ. The chosen values $f = 10\%$, $\chi = 1\%$, and $S/N = 1$ serve hereby as reasonable starting values, which are within the vicinity of a feasible experiment.

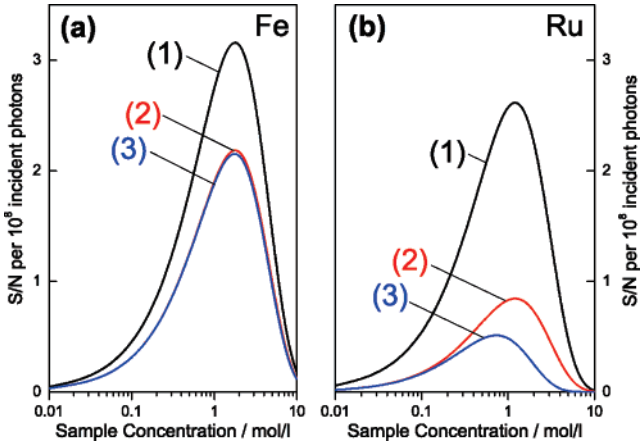

Figure 8. S/N as a function of sample concentration for aqueous solutions of $[Fe^{II}(bpy)_3]^{2+}$ (a) and $[Ru^{II}(bpy)_3]^{2+}$ (b): (1) the result for the metal atom without ligands and solvent, (2) in an aqueous solution without ligands and, (3) in an aqueous solution including ligand and counterion (here $2Cl^-$) contribution (see the text for details).

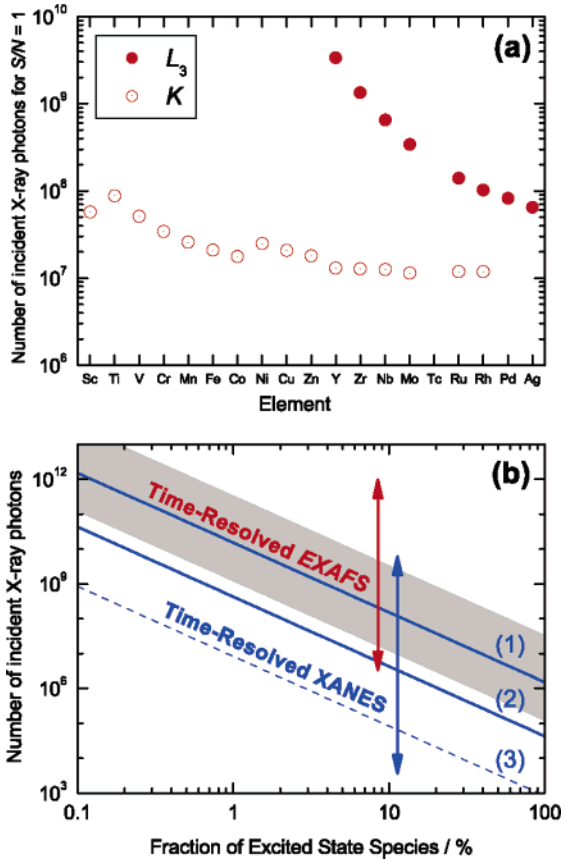

Figure 9. (a) Required number of incoming X-ray photons to observe time-resolved EXAFS of transition-metal compounds in H_2O solution with a signal-to-noise ratio $S/N = 1$. No ligand or counterion contributions were included (see Figure 8). Input parameters are $f = 10\%$, $\chi = 1\%$ (relative to the absorption edge jump of the selected element). The maxima of curves 2 in Figure 8 for Fe and Ru correspond to the data points for these elements. (b) Feasibility range for time-resolved X-ray absorption spectroscopy. The shaded region indicates the required X-ray dose per data point as a function of the fraction of activated species for the calculated EXAFS experiments on transition-metal compounds shown in part a. Curves 1−3 are extrapolated from experimental results (see section 6.3 for details) of time-resolved XANES.

The sample thickness was chosen to obtain optimized sample concentrations in the 0.1−2 mol/L range. Sample restrictions, e.g., solubility limits, may require even more dilute concentrations, and we will treat such a case in section 6.3 in more detail. Without a priori knowledge of the actual sample (and its response to photoexcitation) and its solvent (including guest−host interactions) it may appear impossible to calculate pump−probe signals. However, under certain conditions we can obtain quite useful results. First, we will consider H_2O as a prototype solvent. Changing the solvent to other first-row solvents (e.g., acetonitrile, hexane) will not seriously affect the results due to their rather similar absorptions in the hard X-ray domain. Heavier solvents, however, e.g., CCl_4, could seriously alter the results and are not applicable to the results shown below. Without knowing the actual sample we can nevertheless obtain quite accurate results, if the sample absorption remains comparable to the solvent absorption of the displaced volume. For hydrocarbons-containing samples this is usually the case, and we will demonstrate this for two example species, ruthenium−tris(bipyridine) and iron−tris(bipyridine).

Figure 8 shows the S/N as a function of sample concentration for both species. For each sample we have calculated three cases: case 1 displays the dependence for a hypothetical sample containing only the central atom neglecting solvent contributions and the residual sample atoms, case 2 shows the central atom only in a water environment, and case 3 shows the full calculation including the water solvent and the three bipyridine ligands. The calculations were performed around the Fe K edge (ca. 7.1 keV) and the Ru L_{III} edge (ca. 2.84 keV). For iron we see that introducing the water solvent (with $d = 0.5$ mm) decreases S/N by less than a factor of 2, since the solvent transmission is quite high at this X-ray energy. Introducing the entire $[Fe(bpy)_3]^{2+}$ molecule including two Cl^- counterions delivers nearly the same result as without the ligand, since the difference in absorption between H_2O and the sample ligands and counterions is very small. This is a little different when calculating $[Ru(bpy)_3]^{2+}Cl_2^-$ dissolved in water (Figure 8b). Since water already absorbs 90% of the incoming X-radiation at the Ru L_{III} edge, curves 1 (without solvent) and 2 (with solvent) differ by a factor of 3. If we introduce the entire sample with ligands and counterions, we obtain a modified curve 3, which has a reduced S/N value and a smaller optimized concentration. This results mainly from the rather strong Cl absorption (cross section) around 2.84 keV. It clearly reduces the signal-to-noise ratio and, according to eq 11, it also optimizes at a somewhat lower concentration in order to obtain the ideal sample-only transmission around 10%.

Both cases, however, illustrate that we can obtain very reliable results for K edge elements with absorption edges above ca. 5 keV, while for L edges around 2.5 keV we might overestimate the maximum S/N value by up to a factor of 2, which is therefore not too much different from the simple case calculated with the metal atom only in the H_2O solvent. Figure 9a shows the results for a selection of transi-

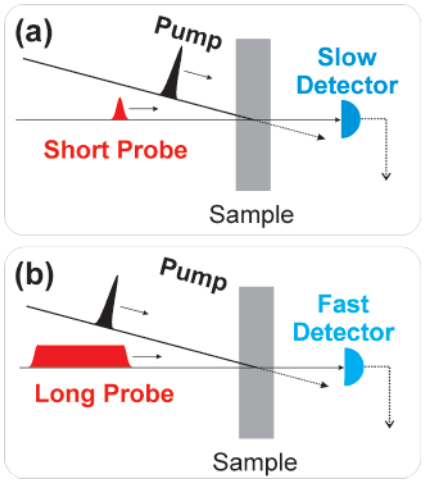

Figure 10. Pump−probe strategies to reach subpicosecond time resolution with X-rays: (a) two ultrashort optical and X-ray pulses and a slow detector and (b) an ultrashort optical pulse and a relatively long X-ray pulse synchronized to a fast detector (e.g. a streak camera; see Figure 11).

tion metals with absorption edges in the 2−22 keV range. For the L edges the sample thickness was kept constant at $d = 0.1$ mm, while for the K edges the thickness was changed from 0.3 mm (Sc), over 0.5 mm (Ti−Co) and 1 mm (Ni−Mo) to 2 mm (Ru and Rh), to maintain the optimum concentration in the 0.1−2 mol/L range.

The results in Figure 9a are displayed in the shaded region in Figure 9b, where the required number of X-ray photons to achieve $S/N = 1$ are plotted as a function of photoexcitation yield f. Each experiment (element) will exhibit an f dependence on a curve parallel to, e.g., curve 1 in the figure, according to eq 13. Thus, the shaded region includes the range of curves obtained for the transmission metals, as shown in Figure 9a, whose data points would be found at $f = 10\%$ in Figure 9b. The shaded region thus displays the feasibility range for time-resolved EXAFS, and the vertical arrow indicates the expected range in general. Time-resolved XANES usually exhibit larger signals, thus their feasibility range should lie at somewhat smaller X-ray doses. Curves 1−3 were generated from experimental data on the transient XANES of a solvated organometallic complex (aqueous $[Ru(bpy)_3]^{2+}$; see section 6.3 for details). Curve 1 displays the result for $S/N = 85$, while curve 2 corresponds to a single scan with $S/N = 7$. Indeed, they are shifted as expected due to eq 13, and curve 3 displays the feasibility limit for this system with $S/N = 1$. From this figure we can see that ultrafast XAS studies can be envisioned with as little as 10^6−10^8 X-ray photons per data point from the source. Below we will show that current and near term pulsed X-ray sources already offer sufficient pulse intensities to accumulate this dose in a reasonable collection time.

5. Ultrafast X-ray Sources and Detectors

After treating in detail the experimental constraints, we will review the state-of-the-art of both sources and detectors and give a preview of X-ray instrumentation that will become available in the near term, i.e., within the next 2 years or so. New large-scale facilities are also in the construction stage, which will offer revolutionary conditions for femtosecond X-ray science (see section 7). With today's technology, there are two strategies to carry out ultrafast laser pump−X-ray probe studies, which are depicted in Figure 10. The first one (Figure 10a) uses an ultrashort optical pulse and an ultrashort X-ray pulse, just as in standard optical-only pump−probe experiments. The second strategy (Figure 10b) uses an ultrashort laser pulse and a relatively long X-ray pulse that is streaked by a fast detector after the sample to deliver information on ultrashort time scales. (Streak camera detectors are discussed in section 5.3.)

For ultrafast XAS, the X-ray source should meet the following requirements: (1) It must provide continuum radiation (since energy spectra need to be scanned), ideally from the soft to hard X-ray region; (2) It should provide ultrashort pulses (unless ultrafast X-ray detectors are used in the experiment; see section 5.3); and (3) It should have a sufficient photon flux, along the considerations developed in the previous section (e.g., as displayed in Figure 9). The efforts to generate ultrashort pulses of X-radiation have followed two main avenues: laboratory-based sources and large-scale installations. The lab-based sources consist of three types: X-ray diodes, high harmonic generation, and laser-generated plasma sources. Their basic characteristics are given in Table 1.

5.1. Laboratory-Based Sources

5.1.1. Laser-Driven X-ray Diodes

These diodes are in principle very similar to rotating anode sources with a thermionic electron source, but they use a laser pulse to generate photoelectrons from a photocathode. These are then accelerated to several tens of kiloelectronvolts and generate characteristic line emissions and continuous bremsstrahl-

Table 1: Status of Current and Future Sources of Ultrashort X-ray Pulses

source	availability	photons/pulse/0.1% BW	pulse width	energy range	repetition rate
high harmonic generation	now	10^4−10^6	≥100 as	<500 eV	≤1 kHz
laser-generated plasmas	now	10^1−10^5 (depends on X-ray optics)	100−300 fs	≤30 keV	10 Hz−2 kHz
third-generation synchrotrons	now	10^4−10^6	20−100 ps	0−100 keV	≤500 MHz
slicing scheme at a bend magnet	now	10^1−10^3	∼100 fs	0−100 keV	1−10 kHz
short pulse photon source (SPPS)	now	10^8	∼100 fs	fixed energy (8 keV)	10 Hz
energy recovery linac (ERL)	ca. ≥6 years following funding	10^4−10^7	∼100 fs	0−100 keV	≤10 kHz
X-ray free electron laser	ca. 2008/2010	10^{11}−10^{12}	∼100−200 fs	keVs	100−500 Hz

ung at the target anode. With 100 fs optical pulses an X-ray pulse width around 1−2 ps was already demonstrated,[112] thus extending the efforts with nanosecond and picosecond lasers by Rentzepis et al.,[43,113−118] Derenzo et al.,[119] and Girardeau-Montaut et al.[120] This technique delivers continuum spectra, but it is not very widespread due to its low efficiency. So far only one group has recorded an X-ray absorption spectrum ∼10 ns after the pump pulse with such a source.[43] In principle, with a sophisticated design including electron optics, the pulse width can be reduced to close to that of the exciting laser.

5.1.2. High Harmonic Generation

Its principle is based on focusing an ultrashort laser pulse onto a gas target (usually a rare gas), which then generates harmonics of the fundamental frequency up to the XUV. These sources are (currently) limited to energies up to about 400 eV.[121−123] However, they deliver extremely short pulses, even down to hundreds of attoseconds duration. To achieve this, one irradiates a gas (e.g., neon) with 5 fs visible light pulses that spark collisions between the neon nuclei and their ionized valence electrons, thus generating outbursts of soft X-radiation of subfemtosecond duration, but for a few shots per pump cycle.[124−126]

Femtosecond and attosecond soft X-ray pulses are finding major applications for the study of nuclear and electron dynamics in atoms and molecules and at surfaces (see section 6.3 and refs 127−137). For structural dynamics research in condensed phase media, however, higher photon energies in the 2−20 keV region are required.

5.1.3. Laser-Generated Plasma Sources

For entering the hard X-ray domain, i.e., photon energies well above 1 keV, a high-power femtosecond laser beam is focused onto a metal or liquid target.[138−148] The generated plasma gives rise to bursts of hard X-radiation. Depending on the technical details of the exciting laser and the target, one can optimize either the continuum portion of the radiation, which extends up to several tens of kiloelectronvolts, or the (more intense) line emission (Kα and Kβ) of the target element(s). These sources are isotropic, but pulse widths of a few hundred femtoseconds have been reported. The performance of these sources in terms of flux also strongly depends on the X-ray optics for collecting the isotropic emission. Today, with one pioneering exception,[149] most applications have exploited the more intense line emissions with flat X-ray optics, thus limiting the available pulse intensity. The femtosecond laser used to generate the plasma runs usually at 10 Hz repetition rate. Rose-Petruck et al.[148] and Hatanaka et al.[142,143] have demonstrated X-ray plasma generation at kHz repetition rates. However, it still needs to be shown that the considerably lower pulse intensities at kilohertz repetition rates can be used for time-resolved XAS studies.

5.2. Large-Scale Installations

Large-scale facilities have well-established schemes to generate highly brilliant and tunable X-radiation. The extraction of ultrashort X-rays from powerful accelerators is mainly focusing on three schemes, which we will discuss below: synchrotron radiation (SR) sources, SR supplemented with the time-slicing scheme, and X-ray free electron lasers (X-FELs). New and exciting schemes at large-scale installations are currently in the design stage and will be discussed in section 7. In this section we present the current state-of-the-art and sources available in the short term.

5.2.1. Synchrotrons

Synchrotron radiation has become the standard tool for measuring high-quality X-ray absorption spectra. In a synchrotron, relativistic electron bunches are cycled and accelerated in a storage ring and used to emit X-ray pulses from bend magnets or insertion devices (periodic magnetic structures such as wigglers and undulators). Synchrotrons represent the most widely used source of X-radiation because of their tunability and brilliance. However, they are limited in performance due to the physics of equilibrium processes fundamental to the operation of storage rings. e.g., the pulse width (the equilibrium length of a stored electron bunch) is limited to the 20−100 ps range. Reducing the pulse duration of a stored electron bunch is practicably impossible, because such short bunches create wakefields and coherent synchrotron radiation, which lead to bunch lengthening and instabilities as they propagate around the storage ring.[150]

5.2.2. The Slicing Scheme

One of the schemes being developed to extract femtosecond X-ray pulses from a storage ring is an add-on to the synchrotron, called a slicing source. It is based on the generation of femtosecond X-rays by scattering a femtosecond laser pulse from a relativistic electron bunch. The ultrafast laser pulse copropagates with the electron bunch inside the storage ring and slices out a wedge of electrons from the 100 ps long bunch. This small slice of electrons consequently produces a shorter pulse of X-rays at an extraction device, possibly as short as 50−100 fs. Since it underlies the same equilibrium processes as the remaining 100-picosecond bunch, it will eventually smear out and merge into the latter. This necessitates the continued production of fresh time-sliced pulses with the femtosecond laser. Schoenlein and his group pioneered this scheme at a bend magnet beamline of the Advanced Light Source in Berkeley for a repetition rate of 1 kHz.[151−154] While this scheme does deliver ultrashort pulses, its disadvantage is that it discards most of the electrons in the original electron bunch and, as a result, the femtosecond X-ray beam it produces is only a thousandth of a typical SR pulse. Furthermore, its extraction from the large pedestal due to the picosecond X-ray pulse is still problematic.

5.2.3. Free Electron Lasers

In contrast to storage rings, the beam emittance and bunch length in a well-designed linear accelerator (linac) are controlled entirely by the particle

source preceding the linac and not by a dynamic radiation equilibrium time of several thousands of periods around the storage ring. Replacing the conventional synchrotron radiation storage ring with a single-pass linac will thus preserve the ultrashort pulse duration, and with the help of two undulators in series, one can generate an intense monochromatic X-ray pulse in the first undulator and seed this radiation in to the second undulator, which will be amplified up to 10^{12} photons per pulse (see section 7). In the short term, a scheme has just recently come into operation in Stanford whereby electron bunches are fired down the SLAC linac to generate femtosecond X-ray pulses with the help of a wiggler. At the end of the wiggler, the radiation adds up to as much as 10^8 photons/pulse in 100−200 fs. This *short-pulse photon source* (SPPS) operates, however, at a fixed wavelength and with a rather low repetition rate (∼10 Hz).[155] Nevertheless, its bandwidth of around 1% corresponds to some tens of electronvolts around the Ni K edge absorption and could therefore be used in a XANES measurement with 100 fs resolution.

One of the crucial parameters in deciding for a plasma source or a synchrotron is the figure-of-merit in terms of tunability, pulse width, and pulse intensity (Table 1). Tunability is a powerful characteristic of synchrotrons and one of the main reasons of their widespread use. Plasma sources are currently the shortest sources of hard X-rays, but SPPS may prove to have shorter and more intense X-ray pulses. SPPS is a single-wavelength source, and laser-driven plasmas are also usually operated only on one single line emission. The issue of comparing intensities is not easy, due to their striking differences in operation. We will attempt a comparison on the following grounds: Although plasma sources are isotropic in nature, they do contain an appreciable amount of hard X-ray pulse intensity within only a few hundred femtoseconds, which can amount to ca. 10^{11} photons/Å^2 for 1 J of laser pump energy.[145] This value now refers to the weaker broadband continuum emission available, e.g., in the 2−10 keV range. The drawback of isotropic emission can be solved, if one could use sophisticated X-ray optics capable of collecting a reasonable solid angle and dispersing monochromatized radiation onto an area detector (thus collecting in a dispersive mode an entire XAS within one single shot). A conservative estimate then yields a pulse intensity of around 10^1−10^5 photons/pulse/0.1% bandwidth for reasonably sized X-ray optics,[147] which is comparable to the pulse intensities extracted from third-generation synchrotrons. However, due to the dispersive arrangement, this pulse intensity (e.g., per electronvolt bandwidth) is available for an extended energy range covering several hundred electronvolts. Thus, with the constant optimization in the performances of plasma-based sources and the fact that they already deliver X-ray pulses of femtosecond duration, these could become one day routine lab-based sources for ultrafast XAS experiments, provided the adequate X-ray optics are available.

5.3. Detectors

As shown in Figure 10b, another solution to reach the highest possible time resolution is to streak the tens of picosecond long X-ray pulse from a synchrotron (or from other sources) in a streak camera, after it has traversed the sample. The principle of the streak camera operation is shown in Figure 11. It is based on converting the X-ray pulse at the photocathode into an electron pulse of the same duration, which is then accelerated to a few tens of kiloelectronvolts and "streaked" by a pulsed electrostatic field onto an area detector (e.g., CCD), thus distributing the temporal information within the X-ray pulse spatially (vertically, Figure 11) onto a streak image. The time resolution is limited mainly by the initial electron energy dispersion at the photocathode (PC) and the temporal broadening of the electron bunch affected by the Coulomb repulsion during its travel to the phosphor screen at the CCD camera, including the transit time dispersion induced by the electron focusing optics and the geometrical arrangement. Simulations have shown that subpicosecond time resolution can be reached with a few electrons in the electron bunch.[28] The main drawback of current streak cameras is their currently low sensitivity, on the order of 0.1%, which necessitates more intense X-ray sources for widespread use.

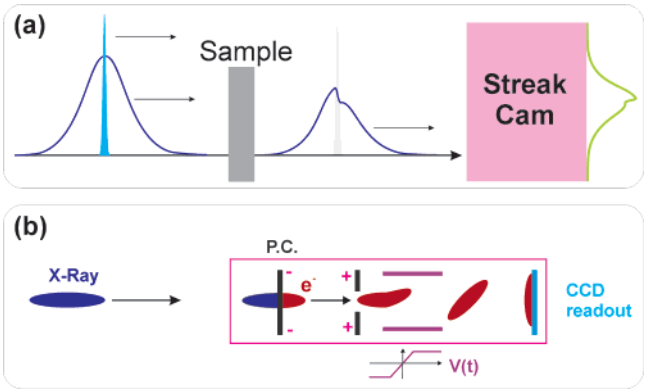

Figure 11. Principle of a streak camera. (a) The pump laser is set at the maximum of the time distribution of the (Gaussian-shaped) X-ray pulse. Thus, any changes in sample transmission following the optical pump pulse will modify the temporal X-ray intensity distribution after the sample. (b) After it has transmitted the sample, the X-ray pulse reaches the photocathode (PC) of the streak camera and produces a bunch of electrons, whose density reflects the temporal intensity profile of the X-ray pulse. A ramped field ($V(t)$) triggered by the same laser used for exciting the sample streaks the horizontally aligned electron bunch into the vertical axis as a function of time. The deflected electron bunch reaches a phosphor equipped with a CCD readout. The (horizontal) time axis is thus converted into a (vertical) space axis.

Paradoxically, while a huge and costly effort is being invested in the development of sources of ultrashort X-rays, the activity in terms of ultrafast X-ray detectors is deceptively low. Maksimchuk et al reported the operation of an X-ray streak camera having a resolution of about 20 ps.[156] Falcone and co-workers in Berkeley pioneered the use of an ultrafast X-ray streak camera to chop out ultrafast information from the 70 ps X-ray pulse at a synchrotron, in X-ray diffraction and recently even in soft X-ray absorption experiments[56,157−161] (see section 6.3). They achieved an impressive time resolution of around 2 ps. Kieffer and co-workers[162,163] demonstrated the operation of

an X-ray streak camera with 350 fs time resolution, but the low photocathode quantum efficiency (ca. 0.1−1%) most likely hampers its use for ultrafast X-ray absorption spectroscopy.

This short review of ultrafast X-ray technology shows that for the time being (<6 years from now, Table 1), only rather weak subpicosecond tunable hard X-ray sources will exist for time-resolved XAS studies. However, along the lines developed in section 4.2, experiments are feasible after a careful consideration of the interplay between pump laser, sample design, X-ray probe, and X-ray detection. The continued progress on new sources and improved detectors makes us hopeful that the situation will change in the next 6−10 years (see section 7).

6. Time-Resolved XAS Studies

Ultrafast time-resolved XAS is a nascent field, and many efforts are still needed to fully establish it as a routine technique. However, along with the considerations developed in the previous section, we feel that the knowledge and expertise built from early studies with time resolutions of microseconds to nanoseconds offer a background on which present and future experiments can be envisioned. In the following, we will review the studies carried out on different types of systems used, by starting from long time scales down to the shortest ones.

The development of energy-dispersive XAS at synchrotrons, coupled with sensitive detectors, has allowed the recording of entire spectra (over hundreds of electronvolts) on the tens of microsecond time scales. This has been applied to slow (diffusion-limited) chemical reactions in solutions.[164] However, such experiments generally do not take advantage of the time structure of the source but rely on its high average flux (e.g., at synchrotrons) to decrease data collection times. More relevant to the present review are experiments where the time structure of the X-ray source is exploited by synchronization with an external trigger that induces some electronic or structural changes on the system of interest (e.g., by absorption of light).

Historically, the first attempt of this sort was carried out by Cohen et al.[165] They used the time structure of a synchrotron source (repetition rate 1−28 MHz) in the hard X-ray regime and a nanosecond gated detector to discriminate between electronic (scattering) and nuclear (Mössbauer fluorescence) events. The latter have long lifetimes (∼100 ns), whereas the former occur during the X-ray pulse. We mention this example here not only for historical reasons but also because Mössbauer spectroscopy is an extremely powerful tool used in structural research,[166] which may even be viewed as an analogue to XAS in nuclear spectroscopy. We feel its extension to time-resolved studies, especially in the short time domain, could open a new area of research in structural dynamics.[167]

In the following, we review the studies that were carried out using the pulsed nature of the X-ray source, descending from the microsecond time domain to the femtosecond time scale.

6.1. The Millisecond to Microsecond Time Domain

6.1.1. Biological Systems

It is interesting to note that the first attempts at using time-resolved XAS dealt with biological systems. The pioneering studies in time-resolved XAS were carried out by Mills and co-workers,[168−173] who studied a photobiological reaction, namely, the dissociation of the CO ligand from carboxymyoglobin (MbCO) and its recombination over time scales of micro- to milliseconds. To this aim, they developed a scheme synchronizing a Nd:Yag laser used for the photolysis of MbCO with bursts of X-ray pulses from the synchrotron CHESS at Cornell for probing the X-ray changes in the edge region (i.e. XANES) of the K shell of the iron atom near 7 keV.

As discussed in section 3.2, the energy position of the absorption edge is sensitive to the local environment of the absorbing atom, and one observes shifts of several electronvolts, as both the species and distribution of the atomic neighbors are altered. This effect is clearly visible in Figure 12a, which compares the static XAS of the unligated protein (deoxymyoglobin, Mb) and the ligated one (carboxymyoglobin, MbCO).[170] Mills and co-workers used this energy shift to monitor the recombination of the carbon monoxide molecule with the iron atom after laser flash photolysis. Figure 12b shows four time-resolved XANES spectra collected in fluorescence mode (see section 3.3) for a 1 mM Mb solution. Each spectrum is compared with the spectrum of the reactant MbCO complex (black lines). The main differences arise from the fact that the preedge feature at ∼7.104 eV is more pronounced in Mb−CO and the main edge is shifted to higher energy. The preedge feature is due to a dipole-forbidden 1s−3d bound−bound transition (see section 3.2), while the main edge absorption is due to the 1s−5p transition. The position of the deoxymyoglobin X-ray absorption edge in the top two spectra is clearly shifted toward lower energy relative to the MbCO spectrum, signifying that a substantial fraction of the carbon monoxide has not yet recombined with the myoglobin. The third spectrum in the figure gives an indication of near-complete recombination. By the time the fourth spectrum was recorded, the curves are nearly identical, indicating complete recombination.

While these results represented a breakthrough and demonstrated the applicability of time-resolved XAS to photobiological processes, the details of the spectroscopic changes were not discussed. In particular and in line with section 3.2, an edge shift generally suggests a change in the oxidation state of the Fe atom, while the preedge feature suggests a lowering of symmetry of the porphyrin reaction center from the deoxy to the carboxy form of myoglobin.

Similar studies on Mb−CO were pursued by Clozza et al[174] and mainly by Chance and co-workers,[175] also using synchrotrons as the X-ray source. Clozza et al developed an apparatus that used the synchrotron as a quasicontinuous source, where the data acquisition was triggered by the laser and carried out for

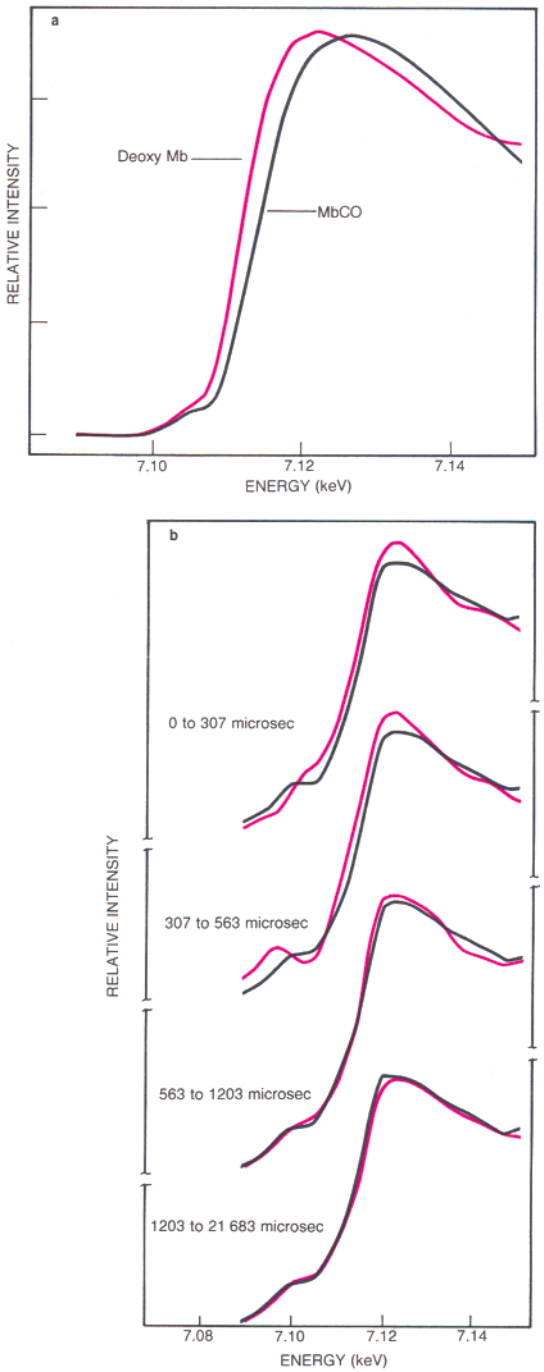

Figure 12. Static and time-resolved XANES spectra of iron in deoxymyoglobin (Mb) and carboxymyoglobin (MbCO). The top panel (a) contains the static spectra, which show that the addition of the CO ligand causes a shift in position by about 3 eV of the iron edge, relative to deoxymyglobin. The lower panel (b) shows the time-resolved spectra, compared to the static reactant spectrum of MbCO. The clear shift in energy of the absorption edge seen in the upper two spectra indicates that a large fraction of the photolyzed CO has not yet recombined with the myoglobin. The time intervals after the laser pump pulse, during which the data was recorded, are shown on the left. Reprinted with permission from ref 170. Copyright 1984 American Institute of Physics.

well-defined time delays using time windows down to the millisecond time scale. The apparatus was designed to detect X-ray fluorescence (rather than transmission), thus allowing work on rather dilute samples. Furthermore, low temperatures were used to slow the recombination process of CO with Mb and thus to trap intermediates. A slightly modified setup was developed by Chance et al,[175] allowing them to collect time-resolved XAS spectra in the millisecond time domain for very dilute samples (1−4 mM). Parallel to these efforts, Chance and co-workers[176−179] carried out systematic XAS studies of the photolyzed MbCO and also Mb−O_2 and deoxy-Mb, using low temperatures (<10 K) in order to trap the photoproducts. These studies used continuous (cw) light sources for photolysis and did not exploit the time structure of the X-ray source. However, along with the above-mentioned work, they do demonstrate the power of XANES and EXAFS for determining electronic and structural changes in biological systems. In particular, they show that

(i) one can work at very low concentrations down to 1 mM;

(ii) one can use both K- and L-absorption edges;

(iii) working in fluorescence mode with adequate detectors allows one to discriminate between edge fluorescence and background scattering, thus enhancing the overall sensitivity; and

(v) the precision of structural determination via EXAFS is 1 order of magnitude larger than in comparable diffraction studies. It can therefore be used to cross-check the physiological validity of the latter, since the XAFS experiments are performed in solution phase and not on artificial protein crystals.[178]

6.1.2. Coordination Chemistry

Time-resolved energy-dispersive XAS was applied to the study of photoinduced reactions in coordination chemistry. Photoinduced electron-transfer reactions were studied by Chen et al.[180] in the case of a diporphyrin within a modified heme protein. They determined the photoinduced electron transfer from the lowest excited triplet state of a Zn−porphyrin attached to an Fe(III)−porphyrin by a 25 Å long spacer. They could observe, over milliseconds, the transient reduction of Fe(III) to Fe(II) by XANES, accompanied by substantial weakening of the bond between the Fe atom and a pyridine molecule ligated to it.

Thiel et al.[181,182] studied the photoinduced structural changes of $Pt_2(P_2O_5H_2)_4^{4-}$ in solution in its triplet state (lifetime 4 ms), using a cw Ar^+ laser at 363 nm and a synchrotron as the X-ray probe source. The timing between the laser and the X-ray was done using an elegant experimental method that consisted of exciting the liquid jet sample in a region whose height with respect to the probe beam was finely tuned, so that with the defined liquid jet velocity the time delay between laser pump and X-ray probe could be adjusted down to the millisecond time domain.

It is interesting to note once more that these pioneering studies were mainly carried out on biological systems or coordination chemistry systems, stressing the relevance of time-resolved XAS to unravel details of their function and reactivity. Furthermore, they all exploited X-ray fluorescence detection in order to suppress the background signal, which becomes dominant at low concentrations typical for biological samples (see section 3.3). With the

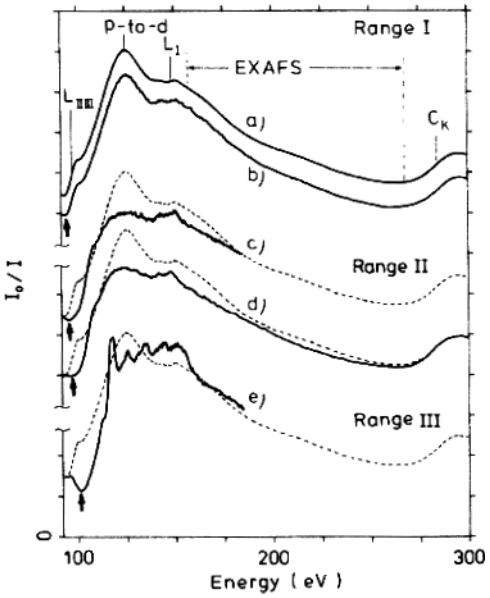

Figure 13. Time-resolved XAS spectra of a Si/C foil, 12 ns after laser excitation, for excitation densities: (a) 0 (no laser), (b) 0.12 J/cm^2, (c) 0.3 J/cm^2, (d) 0.6 J/cm^2, and (e) 3.6 J/cm^2. The edge at 280 eV is due to the carbon foil K absorption. The dotted lines show the reactant spectrum (a) for comparison. The arrows indicate the onset for the Si $L_{II,III}$ absorption. The *y*-axis indicates the ratio of the incident X-ray intensity I_0 to that of the transmitted X-rays, I_1. The pump excitation density effects are separated in three ranges. The peaks in range III correspond to the formation of a plasma. Reprinted with permission from ref 184. Copyright 1986 American Physical Society.

increasing time resolution of XAS experiments, the diversity of systems that can be studied increases, as we now discuss.

6.2. The Nanosecond Time Domain

6.2.1. Material Science

One of the areas where nanosecond resolved XAS was most applied to is material science, to address issues such as laser-induced melting and semiconductor-to-metal phase transitions of covalently bonded semiconductor solids, such as silicon. This is due to both the technological relevance for semiconductor processing and the peculiar structure of the melt: typically, these liquids have coordination numbers of six or seven, values significantly lower than in most liquid metals, where the number of nearest neighbors is on the order of 10 to 12.[183] This lower coordination number is presumably due to a persistence of covalent bonding. Although X-ray and neutron diffraction experiments have accurately characterized the atomic structure of liquid silicon, experimental determination of the electronic structure, which is essential for describing the chemical bonding, was missing. Therefore, already in 1986, Murakami and co-workers[184] used nanosecond pulses of continuum X-rays from a laser-produced plasma (see section 5.1), which provided enough photons in the soft X-ray range (<300 eV) to study the time-resolved L edge spectrum of laser-heated silicon foils. Figure 13 shows the temporal evolution of the L edge spectrum they observed. They interpreted their data qualitatively in terms of a combination of melting and breaking up of the sample into droplets. In particular, the change of the $L_{II,III}$ edges and the overall decrease in absorption were attributed to the metallic character of liquid Si. However, a quantitative interpretation requires higher time resolution, sufficient to distinguish between these very different effects, and more recent results (presented below; see section 6.3) by the Falcone group address this problem.[161]

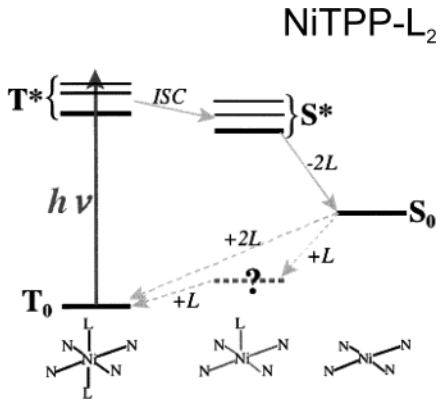

Figure 14. Reaction path following photodissociation of NiTPP-L_2 (only the nearest neighboring atoms that are chelated with Ni are shown), where the ground triplet state T_0 is photoexcited to upper triplet states T* (representing a group of possible triplet states). T* then undergoes intersystem crossing (ISC) to S*, which occurs very quickly, and, finally, ejection of two ligands occurs to form S_0. The laser pump−X-ray probe XAFS experiment captured this transient species, before it returned to the ground state T_0 of NiTTP-L_2 (see Figure 16 and text for a detailed description of the reaction path). Reprinted with permission from *Science* (http://www.aaas.org), ref 186. Copyright 2001 American Association for the Advancement of Science.

The same group extended their studies to the dynamics of laser-ablated particles and the laser ablation/deposition process in the nanosecond time domain.[185] As can be seen in Figure 13, the structures that appear at the largest laser fluences (range III) are due to ablated particles, and this allowed their chemical identification (Si, Si^+, Si^{2+}, ...atoms, Si clusters, and liquid droplets) as a function of distance from the Si surface for time delays between 0 and 120 ns. However, the X-ray probing served in this case only as a spectroscopic diagnostic tool.

6.2.2. Coordination Chemistry

In an important experiment, Chen and co-workers[186,187] studied the transient processes resulting from the photodissociation of NiTPP-L_2 (NiTPP = nickel tetraphenylporphyrin; L = piperidine ligand) with nanosecond time resolution. The photocycle for NiTPP in solution is described in Figure 14. The dissociation reaction is reversible and the photodissociation/association can be triggered by laser excitation. The axial ligands dissociation/association processes of heme-like porphyrin derivatives are examples of how the coordination chemistry of the metal ion (Ni) can be altered by the electronic structure of its macrocycle ligands.

Starting with NiTPP-L_2, a laser pump pulse induces an electronic transition from the triplet state, T* (Figure 14). This state decays and undergoes rapid intersystem crossing to an excited singlet state, S*.

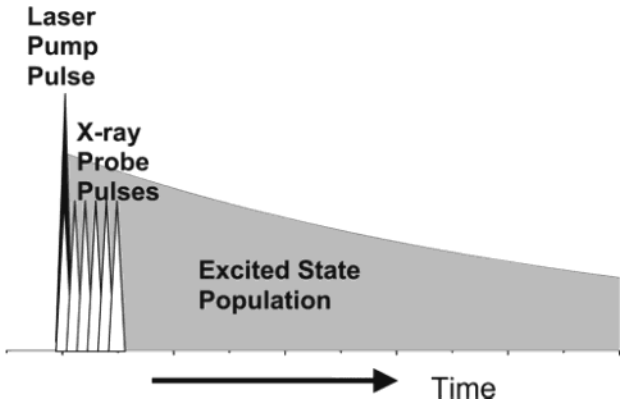

Figure 15. Experimental time sequence used in Chen and co-workers' experiments.[186,188] The laser pump pulse (black triangle) was overlapped with the first X-ray pulse of a sextuplet cluster (white triangles). This time sequence allowed a "snapshot" of the thermally equilibrated excited-state structure to be taken when its population was largest. Reprinted with permission from ref 188. Copyright 2002 American Chemical Society.

The latter state ejects two ligands L to produce the square planar geometry. If the solvent was noncoordinating or weakly coordinating, this reaction sequence would be complete. However, in a strongly coordinating solvent, S_0 is unstable and the system will return to T_0, by recombining with two piperidine molecules, NiTPP-L_2 (Figure 14). Chen et al addressed the issue of the transient structures involved in this recombination, which were not known. A pentacoordinated NiTPP-L molecule could be involved in the recombination, the square planar NiTPP could return to T_0 via a concerted axial chelation with two piperidine molecules, or an intermediate square pyramid NiTPP-L structure could be important. Because it is difficult to identify a unique optical absorption spectrum for each possible intermediate involved in photodissociation, transient optical absorption spectra of NiTPP in the coordinating solvent alone are not sufficient to identify the intermediates. Chen et al probed the transient structures using X-rays from a synchrotron to capture the intermediate on a 14 ns time scale. They used the time sequence depicted in Figure 15 for the pump and the X-ray probe pulses. The laser pump pulse is overlapped with the first X-ray pulse of a sextuplet train of pulses. These six pulses span a duration of 14 ns, allowing one to probe the excited-state structure, given that its lifetime is 28 ns. The XAS spectra are shown in Figure 16 and show the photoexcited spectrum together with both static spectra of NiTPP-L_2 and a photostable form of NiTPP in their ground state for comparison. They could determine the Ni−N bond distance and show that the intermediate species is planar (as ground-state NiTPP) and that no pentacoordination occurs. This is substantiated by the fact that the preedge 1s−3d peak in the XANES is not enhanced, as it should be in the noncentral geometry of a square pyramid NITPP-L complex. Therefore, in the association process, the NiTPP intermediate recombines with two ligands simultaneously (to within 14 ns) in order to form the stable octahedrally coordinated NITPP-L_2.

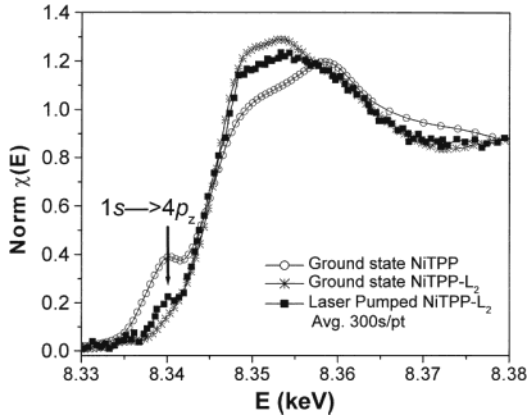

Figure 16. XANES spectra near the Ni K edge, with normalized X-ray absorption $\mu(E)$ as a function of X-ray photon energy E. The shoulder at 8.340 keV that is present in the ground-state NiTPP and in the laser-pumped sample is indicated by the arrow. The XANES spectrum for the laser-pumped sample can be approximated by mixing the ground-state spectra of NiTPP-L_2 and NiTPP with a ratio of 7:3. Reprinted with permission from *Science* (http://www.aaas.org), ref 186. Copyright 2001 American Association for the Advancement of Science.

The same experimental technique was used by Chen and co-workers[188] to study the charge-transfer process of a Copper complex [Cu^I $(dmp)_2$] (BArF), where dmp is 2,9-dimethyl-1,10 phenantroline and BArF is tetrakis(3,5-bis(trifluoro methylphenyl)borate, in toluene. The visible excitation of this complex produces a metal-to-ligand charge-transfer (MLCT) excited state with a 98 ns lifetime. Probing this state within 14 ns after laser excitation with pulsed X-rays shows that a Cu^{II} center in a Cu^I geometry binds an additional ligand to form a five-coordinated complex with increased bond lengths and a coordination geometry of a distorted trigonal pyramid. The EXAFS data shows an increase of the average Cu−N distance by 0.07 Å.

In both of these studies, the detected signal was the X-ray fluorescence, which was recorded as a function of X-ray excitation by a multielement Ge detector, especially developed for this purpose.[189] Nevertheless, typical data acquisition times for recording an X-ray spectrum were ~20 h. Furthermore, in these experiments the time delay between laser and X-ray pulses was fixed and the time window for probing was quite large (14 ns). In an ideal experiment, these two limitations should be overcome in order to be able to probe intermediate states and/or structures in a given photocycle. This is now feasible, thanks to recent advances in the picosecond/femtosecond time domain as discussed below.

6.3. The Picosecond to the Subfemtosecond Time Domain

This part discusses time-resolved XAS studies from femtoseconds to less than 100 ps time resolution. As shown in Table 1, there are nowadays only three types of sources capable of delivering ultrashort X-ray pulses routinely: synchrotrons and laser-generated plasmas, which both cover the soft to hard X-ray domain and high harmonic generation, which is limited to soft X-rays (ca. 10−400 eV). They all have

been implemented for performing femtosecond optical pump−X-ray probe experiments in a few recent pioneering studies, which we now review.

6.3.1. Gas-Phase Studies

In a pioneering experiment, Raksi and co-workers carried out a pump−probe study of the SF_6 molecule using X-rays from a laser-generated plasma already in 1996.[149] The idea to use SF_6 for a demonstration of time-resolved XAS was based on the fact that its near-edge (K and L) X-ray spectrum has very strong absorption features due to shape resonances, thus relaxing the requirements for the X-ray source and the detection system. As discussed in section 3.2, these shape resonances are due to multiple scattering and interference of the photoelectrons by the fluorine atoms symmetrically surrounding the central sulfur atom.[96,190] The increased overlap of the initial, spatially narrow core electron state with the quasi-trapped valence electron state, which is also confined to a narrow radial distribution by the fluorine scattering quasipotential, results in a sharp and intense resonance line in the near-edge X-ray absorption spectrum.[96] In SF_6, the magnitude of the resonance results in an 8-fold increase in the ionization cross section at the K edge near at 2.48 keV (4.98 Å), with respect to the nearby K continuum. This resonance is characteristic of the molecule, not of the sulfur atom itself. As the molecule dissociates, losing F atoms and its high octahedral symmetry, it should greatly diminish or disappear.

The experiment was performed at the K edge of sulfur. The laser-produced plasma on metal targets generated a continuum around 2.4 keV with a 1.5−3 ps pulse duration, as measured by a streak camera. The X-ray absorption spectrum of the unexcited SF_6 molecule is shown in Figure 17a. It was recorded with the molybdenum plasma L emission continuum. A laser pump pulse was used to photodissociate the SF_6 molecule, stripping off its six F atoms upon multiphoton ionization. This leads to the disappearance of the shape resonance seen in Figure 17a.

Figure 17b shows the variation of the X-ray transmission of the SF_6 gas sample at the shape resonance line as a function of optical pump−X-ray probe time delay. The shape resonance of the molecule is strong and clearly resolved in the absence of any pump pulse (Figure 17a), as well as at negative time delays, when the probe pulse arrives before the photodissociating pump pulse. For $t \geq 0$, a bleaching of the X-ray shape resonance is observed, indicating photodissociation of SF_6. Indeed, although the details of fragmentation are not known, none of the possible products are expected to have shape resonances comparable in strength with the original SF_6, since the symmetry and number of coherent scatterers around the S atom is greatly reduced for the possible fragments. This experiment represented not only a technological breakthrough but also demonstrated the intimate link between electronic and structural effects, which we feel is at the core of the high potential of time-resolved XAS in the future.

Visible pump−soft X-ray probe studies of the photodissociation of gas-phase molecules were carried out by Leone and co-workers, using high harmonic generation to produce ultrashort pulses (250 fs) of soft X-radiation (at 26.4 eV). The dissociation of Br_2 was probed by photoelectron spectroscopy following absorption of the soft X-ray pulses.[133−135] Photoelectron spectroscopy does not deliver structures, but this work demonstrates the feasibility of femtosecond X-ray absorption experiments. In a foregoing work, Oguri et al.[191] demonstrated a femtosecond optical−soft X-ray cross-correlator, operating on the X-ray absorption line of optical field-ionized Kr atoms.

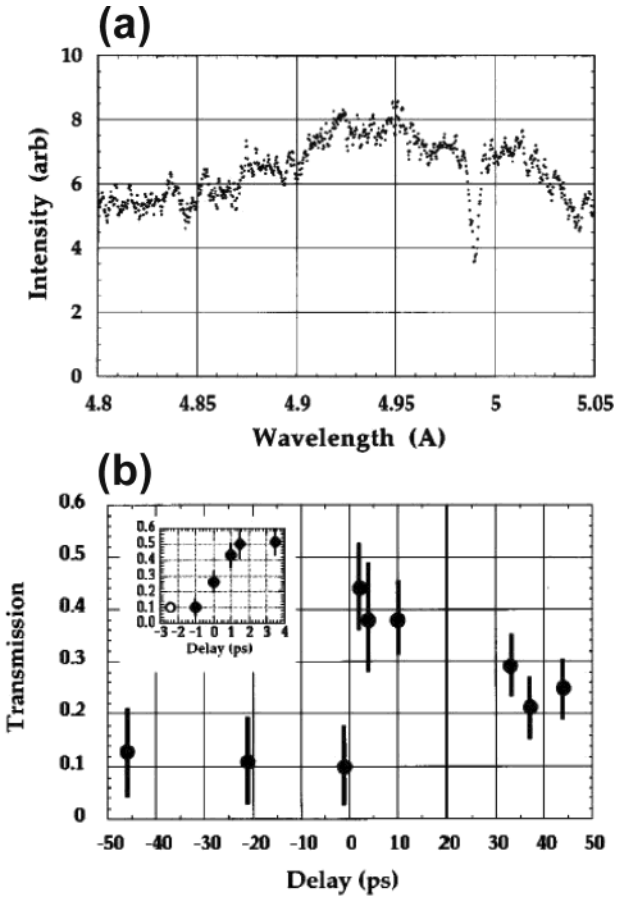

Figure 17. (a) SF_6 shape resonance absorption line measured via the transmitted X-ray intensity through SF_6 gas at 4.986 Å with the quasicontinuous L emission bands generated in a laser-driven molybdenum X-ray plasma source. (b) Transmission of X-rays through the SF_6 gas at the peak of the shape resonance absorption line, as a function of time delay between the pump pulse that initiates photofragmentation of the SF_6 molecules and the probe X-ray pulse. The inset shows an expanded view around zero delay at higher time resolution. The open circle corresponds to the transmission without the pump pulse for comparison. Reprinted with permission from ref 149. Copyright 1996 American Institute of Physics.

In the context of this review, it is also worth mentioning a study using the TTF free-electron laser at Hasylab-Desy, delivering 100 fs XUV pulses, in which Coulomb explosion of Xe clusters was studied. Even through this work was not time-resolved, it does set the stage for future laser pump−X-ray probe experiments at an FEL.[192]

Finally, attosecond soft X-ray pulses are already finding applications for the study of electron dynamics. Krausz and co-workers managed a major break-

through by studying the relaxation dynamics of core-excited Kr atoms, using a subfemtosecond soft X-ray pump pulse and a synchronized few femtosecond visible light probe pulse.[131] The soft X-ray pulse excites a photoelectron from the M-shell, thus creating a vacancy. The latter is subsequently filled by an electron from an outer shell upon emission of a secondary (Auger) electron. Probing the emitted photoelectron and the Auger electron reveals the excitation and relaxation dynamics of the core-excited atom in the hundreds of attosecond time domain.

Soft X-rays are common tools for surface characterization by photoemission and photoelectron spectroscopies.[102] Their extension to optical pump−soft X-ray probe schemes to study ultrafast surface phenomena is underway. Heinzmann and co-workers[193] developed a visible pump−EUV probe apparatus, based on photoemission spectroscopy, capable of a temporal resolution of 100 fs. The latter was determined in a cross correlation between a visible and an XUV pulse monitoring the signal from very fast (≤20 fs) hot-electron relaxation dynamics on a Pt surface. Similar studies on metals have been started by Aeschlimann and co-workers.[194,195] Finally, evidence of a change in the chemical environment of oxygen on a Pt surface was observed in visible pump−soft-X-ray probe photoelectron experiments.[137] Electron emission from metal surfaces has theoretically been considered for a determination of the carrier envelope phase of femto- and subfemtosecond pulses.[196] This work hints to an application of these ultrashort pulses for the study of surface dynamics.

6.3.2. Material Science

Subnanosecond-resolved X-ray absorption spectroscopy has been used to characterize the plasma resulting from high-power laser excitation.[197,198] The principle of these experiments consists of generating a hot quasipointlike plasma source of hard X-rays in place of the sample with a first laser beam, while the sample is excited by another laser beam, which produces a "cold" plasma to be diagnosed. The goal in these experiments was to characterize the plasma as a function of distance from the surface of the target, but not to measure the time evolution of the plasma or ejected material. More relevant to material science are studies in which laser-induced ultrafast electronic and structural changes in the bulk material are being probed by XAS in the picosecond time domain.

One of the first optical pump−soft X-ray probe picosecond experiments was reported by Probst and Haig.[199] They probed the dynamics of unoccupied molecular orbital states of tris(8-hydroxyquinoline)-aluminum. A short (80 ps) laser pulse was used to first photoexcite electrons into normally empty LUMO states, and their time evolution was followed by photoelectron spectroscopy using XUV pulses at 22.4 eV generated by high harmonic generation in an Ar gas. With the laser pump on, an additional feature appears in the photoelectron spectrum, which is due to electrons transiently excited into the LUMO. Its temporal dependence could be recorded, providing a means to unambiguously measure the ultrafast decay of the LUMO.

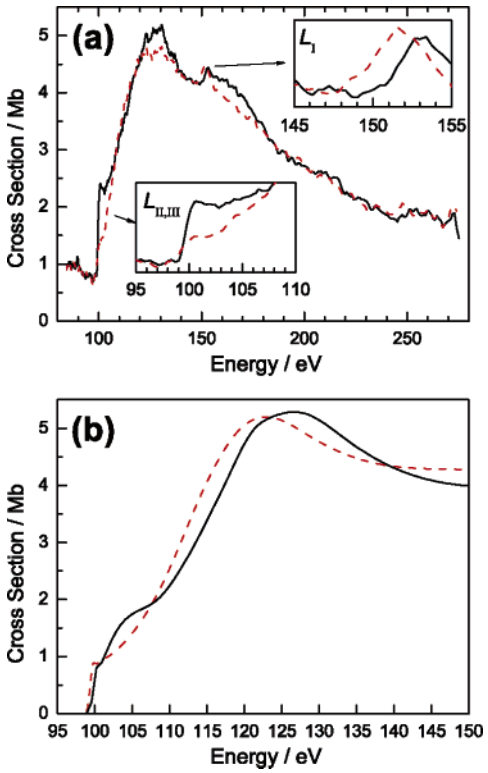

Figure 18. (a) Time-resolved X-ray absorption of a 500 Å thick Si foil, before (dashed curve) and 100 ps after laser excitation (solid line). The $L_{II,III}$ edges at 100 eV and the L_I edge at 150 eV are shown with expanded scales as insets. The plots are an average of 100 laser/X-ray shots, where the foil was translated after each shot. (b) Simulated $L_{II,III}$ edge absorption (see the text) for liquid Si (solid curve) and the unheated Si (dashed curve), for comparison with the experimental traces in a).

Falcone and co-workers[161] have extended to the picosecond time domain the work mentioned above on the semiconductor solid to metallic-liquid phase transition of silicon. They used time-resolved soft X-ray spectroscopy at the Si L edges to probe the electronic structure changes of an amorphous Si foil as it melts following absorption of an ultrashort laser pulse. The X-ray source was the ALS synchrotron in Berkeley, which provided 70 ps pulses dispersed by a plane grating monochromator, whose entire XAS around the Si L edges was recorded within a single shot with an area detector. The experiments were carried out with either a gated set of microchannel plates or, to improve the time resolution, an ultrafast streak camera (see section 5.3), capable of recording changes in the X-ray signal with a 1−3 ps time resolution within a single synchrotron X-ray pulse. A representative pump−probe signal for a 500Å Si foil and an incident laser fluence of 0.7 J/cm^2 is shown in Figure 18a. The dashed curve shows the absorption spectrum before excitation (i.e. the unheated foil). The large edge at 100 eV is a superposition of the L_{II} and L_{III} spin−orbit split edges, which are not separately distinguishable due to the resolution of the spectrometer. At 150 eV, the smaller L_I edge appears. Energies beyond approximately 280 eV were inaccessible, due to beamline filter absorption above the K edge of carbon.

The solid line in Figure 18a shows the absorption spectrum about 100 ps after laser excitation. The

melting induced by the laser causes a dramatic effect at the $L_{II,III}$ edge; the magnitude of the edge is reduced by approximately 50% (see lower insert in Figure 18a). In addition, the near-edge features above the $L_{II,III}$ edge are modified, the L_I edge is shifted to lower energies by 1.6 ± 0.2 eV (see upper insert in Figure 18a), and the small EXAFS modulations beyond the L_I edge disappear. These features remain unchanged until about 10 ns after excitation. Using the streak camera to achieve a higher time resolution (5 ps resolution) of the changes in the $L_{II,III}$, they recorded the integrated postedge absorption as a function of time after laser excitation. The absorption drop is instantaneous within the camera resolution.

The data were interpreted using molecular dynamics (MD) simulations to calculate the atomic structure and ab initio X-ray absorption spectra via the FEFF 8.1 code[200] and to deduce the photoabsorption spectra from this structure. Figure 18b shows a comparison of the model results for the near-edge structure of the $L_{II,III}$ edges for both the initial solid and the liquid. For energies above 110 eV, the model calculations are close to experiment. The prominent feature in this energy range is a broad absorption maximum near 125 eV. This energy shift and the associated reduction of the peak on melting are consequences of the structural changes reflected by the pair correlation function, namely, an increase in disorder and an expansion of the average nearest neighbor distance by 0.15 ± 0.07 Å (compared against the 2.35 Å nearest neighbor spacing in solid silicon). The onset of short-range disorder upon melting also suppresses the EXAFS structure at higher energies via a reduction in the Debye−Waller factor $\exp(-2\sigma^2k^2)$ (see eq 6). Melting causes a large increase in σ, pushing down the EXAFS oscillation amplitude to well below the noise level of the experiment. The observed and calculated shape of the spectrum at these energies is thus consistent with the previously measured structural properties of liquid silicon. Closer to the edge threshold, the agreement is mostly qualitative, possibly due to the neglect of nonspherical components of the electron potential in the FEFF simulations. The MD calculations show that the melting of silicon causes a "flattening" of the density of states (DOS) near the Fermi level and a collapse of the semiconductor band gap. This change in the DOS manifests itself in the spectra as a reduction in the near-threshold absorption, evident in both the model spectra and the experimental data.

The same group carried out a time-resolved XAS study of the bonding in liquid carbon.[201] The properties of the latter are little understood, mainly due to the difficulty of performing experimental studies on liquid carbon, as it requires high temperatures (>5000 K) and pressures (>20 MPa). Therefore, sudden heating of the solid should allow such conditions to be met and a high time resolution would allow the probing of its properties. Optical pump−soft X-ray probe measurements on the carbon K edge for a laser heated foil of "soft" amorphous carbon (α-C) were carried out, and they could follow the time evolution of the proportions of π- and σ-bonding states in the system by recording the changes in the

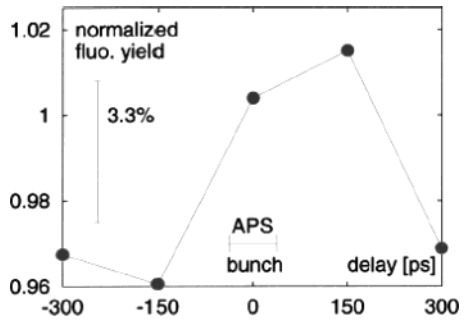

Figure 19. Laser X-ray time delay scan over ±300 ps with 10.637 keV incident photons (and recording the subsequent X-ray emission) from a light-driven GaAs sample. The horizontal bar shows the fwhm bunch length of the X-ray synchrotron pulse. Reprinted with permission from ref 202. Copyright 2002 American Institute of Physics.

XAS spectrum. The studies of the Falcone group on silicon and α-carbon brought the experimental resolution for time-resolved XAS to the picosecond time domain, and they represent a nice example of the amount of electronic and structural information one can extract from ultrafast XAS studies. They also demonstrated its power for quantitatively studying changes in chemical bonding of volatile, high-temperature, near-solid-density materials. Extending such studies to the hard X-ray domain would broaden the field of applications of ultrafast XAS.

Studies of photoinduced electronic changes in semiconductors were carried out by Adams et al.[202] in a picosecond laser pump−X-ray probe study of GaAs, using the Ga Kα X-ray fluorescence following X-ray absorption at the Ga K absorption edge. The aim was to gain direct information on the electronic density of states and the occupation density. In comparison with optical pump−probe techniques, which operate only within band structures and thus yield a convolution over an intermediate state, X-ray spectroscopy allows referencing the pump or the probe process to a discrete level, instead of a band. When a short, intense laser pulse transfers electrons from the valence to the conduction band of GaAs, final states for the Ga K shell X-ray absorption process are vacated in the valence band (VB). Depending on the X-ray energy and where in the valence bands these vacant states are, the cross section for the X-ray absorption (followed by fluorescence) should increase. This process can be used to probe the laser-triggered dynamics of holes in the VB with reference to an absolute energy level (K level of Ga), especially if a narrow band pass analyzer crystal is used for the fluorescent radiation to eliminate the core-hole lifetime effect.[104] The (001) oriented GaAs sample was excited at 4.6 eV by a femtosecond laser and probed with a 150 ps pulse from the APS synchrotron. Figure 19 shows a typical time scan for a fixed incident X-ray photon energy at the Kα edge of Ga. Due to the use of a Si drift detector, the incident intensity had to be limited, which made data acquisition times of several hours per scan necessary. The peak of increased Ga Kα fluorescence in Figure 19 is approximately 200 to 300 ps and is in agreement with typical recombination times in GaAs. This work demonstrates the potential of XAS to improve our

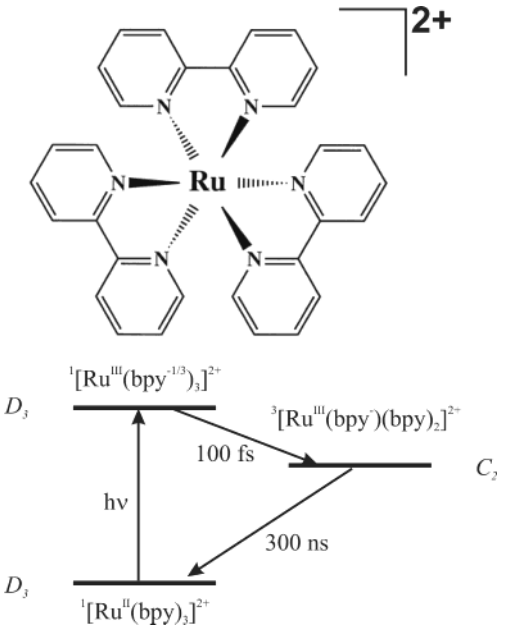

Figure 20. Top: Static structure of $[Ru^{II}(bpy)_3]^{2+}$. Bottom: Photochemical reaction cycle of $[Ru^{II}(bpy)_3]^{2+}$ initiated by excitation of the MLCT transition.

understanding of electronic effects and the dynamics of charge carriers in semiconductor materials.

6.3.3. Coordination Chemistry

When dealing with chemical samples, the highest possible time resolution is required, as one wants to address the elementary steps of a reaction. Furthermore, with nonrenewable samples, a minimization of the data acquisition time is crucial, and the strategy outlined in section 4.2 shows that data acquisition times of durations typical for laser-only experiments are possible. Our group recently demonstrated picosecond-resolved XAS on liquid samples, with very reasonable data acquisition times.[110,111,203]

Aqueous $[Ru^{II}(bpy)_3]^{2+}$ is a model system for metal-to-ligand charge transfer (MLCT) reactions. Its excited-state properties have been readily studied with optical spectroscopies.[204−207] However, little is known about its excited-state structure, which can be investigated via time-resolved X-ray absorption spectroscopy. The reaction cycle is described by Figure 20 (where the superscripts on the left-hand side of the ground- and excited-state compounds denote the spin multiplicity). Light absorption by $[Ru^{II}(bpy)_3]^{2+}$ results in the formation of a Franck−Condon singlet excited state, ^{1}(MLCT), which undergoes subpicosecond intersystem crossing to a long-lived triplet excited state, ^{3}(MLCT), with near-unity quantum yield.[206,207] In the process, the D_3 symmetry of ground state $[Ru^{II}(bpy)_3]^{2+}$ is reduced, in principle, to the C_2 symmetry of $[Ru^{III}(bpy^-)(bpy)_2]^{2+}$ in the ^{3}(MLCT) state.

The oxidation states of (ground state) Ru^{II} and (photoexcited) Ru^{III} complexes exhibit pronounced differences in their L edge XANES.[101,208,209] This is shown in Figure 21a around the Ru $L_{II,III}$ edges. A preedge absorption feature in the L_{III} edge at 2841.0 eV (denoted B in Figure 21) characterizes the bivalent compounds due to the $2p_{3/2} \rightarrow 4d_{3/2}$ (e_g) transition,[101] next to the weaker $2p_{3/2} \rightarrow 5s_{1/2}$ transition around 2851 eV (feature C). Removal of the weakest bound electron from the fully occupied $4d_{5/2}(t_{2g})$ level generates a trivalent ruthenium compound, opening up an additional absorption due to the allowed $2p_{3/2} \rightarrow 4d_{5/2}$ (t_{2g}) (feature A′) in addition to an oxidation state induced shift. Thus, we observe the appearance of the A′/B′ doublet structure in the trivalent L_{III} XANES, together with the energetic B → B′ and C → C′ shift (Figure 21), resulting from the change of oxidation state of the Ru central atom and formation of ^{3}(MLCT) (Figure 21). Below the Ru L_{III} edge we also observe the chlorine K edge absorption due to the Cl^- counterions of the dissolved $[Ru^{II}(bpy)_3]Cl_2$ sample, which does not contribute to the time-resolved experiment.

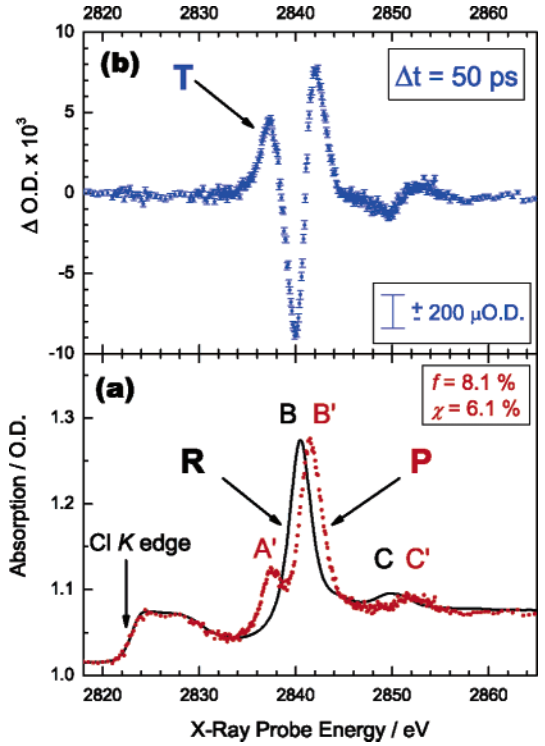

Figure 21. (a) Static L_{III} edge X-ray absorption spectrum of ground-state $[Ru^{II}(bpy)_3]^{2+}$ (trace R), and excited-state absorption spectrum (trace P) generated from the transient data curve T in part b via eq 14. (b) Transient X-ray absorption spectrum (T) of photoexcited aqueous $[Ru^{II}(bpy)_3]^{2+}$ measured 50 ps after laser excitation. Data from refs 111 and 203.

For the experiment we carried out, we exploit a special electron bunch filling pattern of the ALS (Figure 22). The storage ring is filled with several 2 ns-spaced bunches generating a ca. 550 ns long "superbunch", followed by a ca. 100 ns empty section, in which one single electron bunch (the "camshaft" pulse) is placed. This filling pattern allows us to record the intensity of this single X-ray pulse with a suitably fast (and sensitive) avalanche photodiode (APD) detector. The amplified femtosecond laser is synchronized to this camshaft pulse, so that the latter follows every laser pulse at 1 kHz repetition rate and at a fixed time delay. For this purpose the sixth harmonic of the femtosecond oscillator repetition rate is synchronized to the radio frequency of the syn-

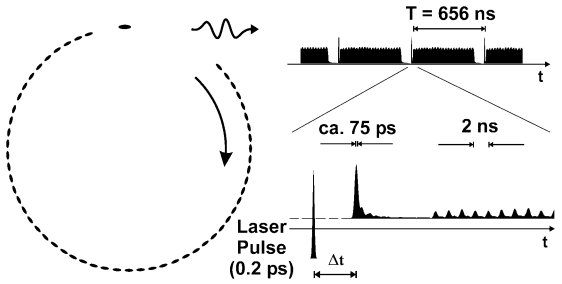

Figure 22. Data acquisition strategy for time-resolved XAS at the ALS−Berkeley. Left: The ALS ring is filled with electron bunches spaced by 2 ns, followed by a 100 ns gap, where only one bunch is found (camshaft mode). This gives rise to the X-ray pulse train shown on the right. Saes et al.[110,111,203] used the camshaft pulse synchronized to the laser pulse (bottom right) and the possibility to vary the time delay Δt between them. The transmitted X-ray pulse is recorded with a sensitive and suitably fast X-ray detector (an avalanche photodiode). Single X-ray pulses are recorded at 2 kHz repetition rate, which allows one to record in situ the dark and photoexcited sample (at 1 kHz rep. rate) on a shot-to-shot basis.

chrotron (500 MHz) with less than 5 ps time jitter. One of these oscillator pulses (locked to the ALS camshaft pulse) is then amplified at 1 kHz repetition rate; thus, the temporal synchronization is maintained. An electronic phase shifter unit allows us to scan the time delay between the laser and X-ray pulses in steps down to ca. 1 ps. The single X-ray pulses are recorded at twice the laser repetition rate (i.e., at 2 kHz), and we monitor—after pairwise subtraction of adjacent X-ray pulse intensities—the transient XAS in transmission mode. This scheme allows us to improve our detection sensitivity to nearly the shot-noise limit of the X-ray source.[107]

Figure 21b shows the actual transient difference absorption spectrum as a function of the X-ray probe energy E, recorded 50 ps after laser excitation (data points with error bars) for a sample containing 80 mmol/L solution of $[Ru^{II}(bpy)_3]^{2+}$ in H_2O. This transient contains all the electronic changes from the reactant state absorption spectrum, $R(E)$, to the product state absorption spectrum, $P(E,t)$, at the time t after photoexcitation. With $f(t)$ being the fraction of excited-state species at time t, the transient absorption spectrum $T(E,t)$ is given by

$$T(E,t) = f(t)[P(E,t) - R(E)] \qquad (14)$$

Thus we can directly deduce the XANES spectrum of the product state from the measured transient signal and the reactant state XAS, if we know $f(t)$. Alternatively, we can derive $f(t)$, if we know the exact shape of the product state XAS, $P(E,t)$. The details are given in ref 203. The resulting spectrum for the $[Ru^{III}(bpy^-)(bpy)_2]^{2+}$ species is shown in Figure 21a (trace P). It contains an energetic shift of all features by 1.2 eV, together with the photoinduced appearance of the A′ feature, as expected. The A′−B′ splitting (4 eV) and the B′/A′ intensity ratio (ca. 2.3) is indeed close to the values observed for $[Ru^{III}(NH_3)_6]^{3+}$ complex,[101,208] which has the same valency and a similar coordination symmetry (O_h versus D_3) as the bipyridine complex.

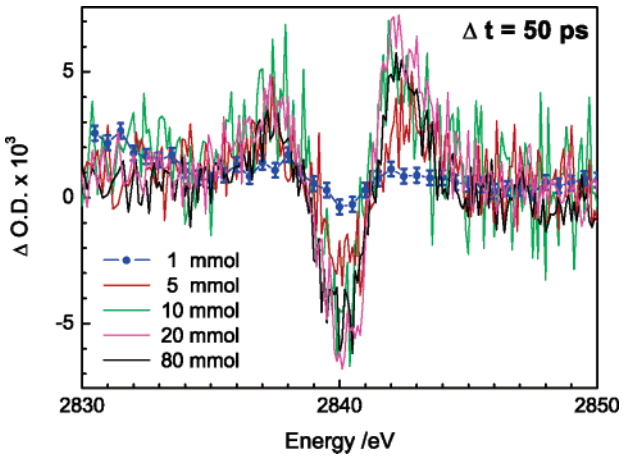

Figure 23. Solute concentration dependence of the photoinduced transient XAS of aqueous $[Ru^{II}(bpy)_3]^{2+}$. All data, except for the 1 mmol/L trace (blue), were recorded under the same experimental conditions (laser intensity and data accumulation time). The lowest concentration sample was recorded with 20 times larger data accumulation time in order to improve the signal-to-noise ratio. All data were recorded during a single energy scan around the Ru L_{III} edge and 50 ps after laser excitation.

The 80 mmol/L concentration used to collect the data in Figure 21 is rather high for typical photochemical studies and gives rise to additional processes occurring on the longer nanosecond time scales.[204] To verify the limits of the experimental methodology along the lines of section 4.2, a solute concentration dependence study was carried out.[111] The results are shown in Figure 23 for different concentrations down to 1 mmol/L and using an increased laser focus, thus reducing the laser intensity (and the photoexcitation yield) in the overlap volume. The spectra represent single scans with 2 s accumulation time per data point, except for the 1 mmol/L sample, which utilized 40 s. Indeed, the error bars of the 1 mmol/L spectrum are a factor of ca. 4.5 smaller than those of the other samples. This is in agreement with a completely shot-noise limited experiment, as discussed in section 4.2. Since the sample thickness was kept constant for all concentrations ($d = 0.1$ mm), the measured transient signal for the 1 mmol/L sample is considerably smaller than for larger concentrations, due to the lower absolute amount of (excited) sample species in the probe beam path. This can be seen from eq 9, which shows that the transient signal is proportional to the product of sample concentration and the fraction of excited state species. For the other concentrations, we observe a roughly equal pump−probe signal, which indicates a concentration-dependent excitation yield. This interesting interplay will be dealt with in a separate publication. The main point here is to emphasize the feasibility of picosecond-resolved XAS studies, even at low concentrations. Below we will compare our experimental results quantitatively, taking the actual flux of the used beamline into account.

A crucial aspect of ultrafast pump−probe spectroscopies is to have the ability to scan the time between pump and probe pulses. This was successfully done for the first time between an optical pump pulse and an X-ray probe pulse in our experi-

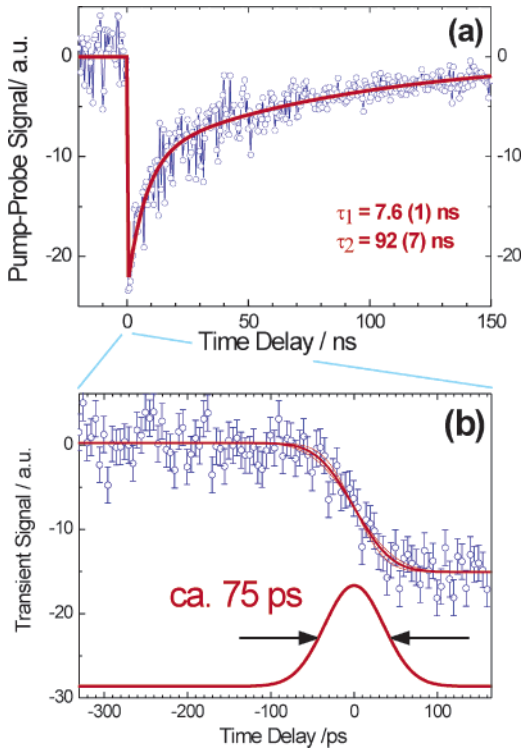

Figure 24. Scans of the pump−probe time delay between the laser pump pulse and the X-ray probe of the transient X-ray absorption signal of $[Ru^{II}(bpy)_3]^{2+}$ (the X-ray energy is set at the minimum of the signal in Figure 21b) over several tens of nanoseconds (a) and in the picosecond time domain (b). The latter represents the cross-correlation signal between the 200 fs laser pulse and the 70−80 ps long X-ray pulse (indicated by the Gaussian-shaped derivative of the fit curve to the data).

ment.[110,111,203] Figure 24 shows an example of such a scan in the nanosecond (a) and the picosecond (b) time domain with the X-ray energy set near the minimum of the signal in Figure 21, thus allowing us to observe the appearance of the photoinduced bleach signal. Once the electron has been excited to the ^{1}(MLCT) state, we can observe the induced oxidation state change of the Ru central atom, and therefore, the time sequence of this pump−probe signal is entirely governed by the cross-correlation time of the exciting laser and the probing X-ray pulses. While this is convenient to both set and confirm the actual timing, we can also exploit this for measuring kinetic traces out to several hundred nanoseconds (Figure 24a), thus allowing a direct comparison with optical-only experiments.[210]

These experiments provide us with quantitative values concerning the required X-ray dose and the achievable signal-to-noise ratio. We will therefore compare these results with the numerical results given in section 4.3. Figure 21 contains an average of 25 spectra, each accumulating for 2 s per data point at 1 kHz repetition rate of the exciting laser. Since we measure alternatively the laser-excited and the dark sample at 2 kHz, we increase the repetition rate by a factor of 2 without compromising the collection time. With our data acquisition strategy we have shown that we can measure the transmitted X-ray pulse intensity via a statistical analysis of the recorded individual X-ray pulses.[110,111] The bend magnet beamline used in this study is specified to deliver a maximum of ca. 9000 photons per pulse at the exit of the double crystal Ge(111) monochromator at 2.84 keV (with a bandwidth of ca. 1 eV), which is reduced to 5300 due to subsequent absorbers (without sample) in our setup. Over the entire storage ring fill time this intensity decreases roughly exponentially by a factor of 3−4, thus yielding on average over several storage ring fills a pulse intensity around 2500 photons per pulse. This compares nicely with the statistical analysis of the measured pulse height distribution of the accumulated single X-ray pulses in a typical energy scan: Over the time following injection we have measured X-ray pulse intensities behind the sample between 80 and 330 photons per pulse, which average to 185 photons per pulse in the case of the 25 scans, which build up the spectrum shown in Figure 21. Correcting this value for the sample transmission yields an *incoming* pulse intensity of 2330 photons per pulse, which is very close to the beamline specification of around 2500. A 2-s collection time per data point at 2 kHz for each spectrum corresponds to a total amount of incoming X-ray photons of 4000 (pulses/data point) × 2330 (photons/pulse) × 25 (scans), yielding 2.3×10^8 photons per data point. The sensitivity level achieved is remarkable: In Figure 21b the error bars are below 200 μOD, which is not easy to achieve in optical-only experiments using amplified femtosecond lasers with many orders of magnitude larger pulse intensities. One important reason for this lies in the extremely stable operation conditions of modern synchrotrons. The flux variation at a beamline end station is dominated by the theoretically calculated shot noise.

The high sensitivity of the transient data is related to the data quality of the product state absorption spectrum shown in Figure 21a calculated via eq 14, and we yield a sensitivity of $\chi = 6.2\%$ (relative to the Ru L_{III} absorption edge jump) for $f = 8.1\%$ (thus for achieving $S/N = 1$). Under these experimental conditions (sample thickness 0.1 mm, and a concentration of 80 mmol/L), we utilized the above derived value of 2.3×10^8 X-ray photons per data point.

This we can scale and compare to our numerical results. Trace 3 in Figure 8b describes the full calculation for aqueous $[Ru^{II}(bpy)_3]^-$ as a function of concentration. For 80 mmol/L we calculate $S/N = 0.136$ for 10^8 incoming X-ray photons, which corresponds to 5.37×10^7 required photons for $S/N = 1$, $f = 10\%$, and $\chi = 1\%$. With eq 13 we now scale these results toward the experimentally determined values in Figure 21a and yield $I_0 = 2.1 \times 10^8$ calculated photons, as compared to 2.3×10^8 incoming photons per data point used in the experiment. The agreement between these values and those of the beamline source specifications is tantalizing and supports the extrapolations drawn for the other transition-metal compounds, as shown in Figure 9b. Curve 1 in Figure 9b has been extrapolated from the measurement shown in Figure 21b. For example, for the dominant XANES transient around 2840 eV, we achieve a signal-to-noise ratio of 85 (peak to peak), while curve

2 corresponds to the single time delay scan shown in Figure 24b, which has a $S/N = 7$. Consequently, photoinduced changes with $S/N = 1$ would be found somewhere along trace 3 in Figure 9b. This not only supports the validity of the numerical results shown in Figure 9a but also demonstrates that that time-resolved XAS can be employed with only 10^6-10^8 incident X-ray photons per data point, and this amount of collected photons lies within the capabilities of subpicosecond X-ray sources to become available in the near future.

This work demonstrated a number of new results and opportunities for ultrafast XAS:

(1) It is possible to work with highly dilute solutions in transmission mode without dramatic loss of signal-to-noise ratio. This is very promising, as one can envision the study of samples for which large concentrations are impossible to reach. Biologically relevant samples are usually investigated in solutions with up to 1 mmol/L concentration (see section 6.1), and we therefore can envision such studies on the ultrafast time scales soon. Furthermore, fluorescence−excitation spectroscopy, which is in principle background-free (see section 3.3), should bring another improvement in signal-to-noise ratio.

(2) It is possible to scan the time delay between the laser pump pulse and the X-ray probe pulse and therefore follow the evolution of the system from the start.

(3) It also demonstrated the operation of an optical-X-ray cross-correlator (Figure 24b).

(4) The time resolution is not a limiting factor, and the experiments are feasible with sources of shorter X-ray pulses, provided the flux is not too low.

In another development, Chen and co-workers[211] extended their time-resolved XAS study of the Copper complex $[Cu^I(dmp)_2]^+$ to the subnanosecond time scale. They were able to capture the structure of the equilibrated MLCT in acetonitrile solution with 100 ps X-ray pulses shortly after laser excitation. Both XANES and EXAFS spectra were recorded. The XANES data show that the copper ion in the equilibrated MLCT state has the same oxidation state as the corresponding Cu^{II} complex in the ground state, and the EXAFS data show that it is pentacoordinated with a shorter Cu−N distance compared to the ground state $[Cu^I(dmp)_2]^{2\bullet+}$. The latter is expected in strong Lewis base solvents, which is the case with acetonitrile. However, in their experiment the time delay between pump and probe pulses was not scanned.

7. Conclusions and Outlook

Ultrafast time-resolved X-ray absorption spectroscopy is a nascent technique that permits the investigation of photoinduced processes on a large variety of systems, on time scales down to the cross-correlation time between the laser and the X-ray pulses. This review has shown the high potential and the present state-of-the-art of research exploiting ultrafast XAS. We have also shown the boundary conditions of the technique and demonstrated that time-resolved XAS can routinely be implemented with reasonable data accumulation times on very dilute chemical and biological samples. Time-resolved XAS is not limited by the time scale, and in reaching the femtosecond domain, we will be able to observe dynamical process including coherent nuclear wave packet motion of complex chemical and biological systems. Undoubtedly, this is one of the most promising applications of femtosecond XAS in chemistry, biology, and material science. Visualizing simultaneously multiple atomic motions in complex systems during the course of a light-triggered reaction would once again revolutionize our view of how Nature functions. The different studies that were so far carried out on chemical systems and on bulk materials have already delivered information that was impossible to retrieve from laser-only experiments. Furthermore, XAS interrogates both the electronic and the structural information on the system.

Like in any other field of science, many advances in ultrafast XAS are driven by technological breakthroughs, and the future is bright! Indeed, new schemes are being proposed and developed, both as far as laboratory-based sources and large-scale installations are concerned (Table 1).[111] For lab-based sources, the main emphasis is on increasing the flux, and a scheme has been proposed[212] to use a prepulse to generate electrons from a molecular beam and to use a second high power femtosecond laser (typically 10^{20} W/cm^2) to simulate an undulator with the electromagnetic field of the laser pulse. This scheme also leads to a somewhat more directed X-ray beam compared to conventional isotropic lab-based plasma sources. However, most of the activity at present aims at generating ultrashort and intense X-ray pulses at large-scale installations, which we now discuss.

Linac-based sources of electrons, called energy-recovery linacs (ERLs) after a concept originally developed by Tigner,[213] are being proposed[214−216] that offer the best performance as a dedicated user facility for producing ultrashort X-ray pulses, at moderate repetition rates in the 1−10 kHz range. In such a facility, electrons are accelerated in a linac to several gigaelectronvolts. The electrons radiate X-rays in a series of conventional insertion devices and are then decelerated in the same linac to recover the energy. The striking advantage of this concept is that it is a single-pass system (each electron bunch passes through the undulators only once). As a result, it is not constrained in the way that a storage ring is by issues such as beam lifetime (scattering losses), bunch instabilities, and emittance degradation, which decrease altogether the pulse width, intensity, and brightness of the radiated intensity.[217,218] These machines promise to fill the gap of necessary ultrafast X-ray sources in the midterm and may become a versatile tool for femtosecond X-ray phenomena in general.

In the mid to far term a completely new type of machine, the X-ray free electron laser (X-FEL), is currently being developed in Hamburg (TESLA) and Stanford (LCLS). These are linac-based machines that will exploit self-amplified spontaneous emission within a long undulator and generate ultraintense monochromatic hard X-radiation with pulse dura-

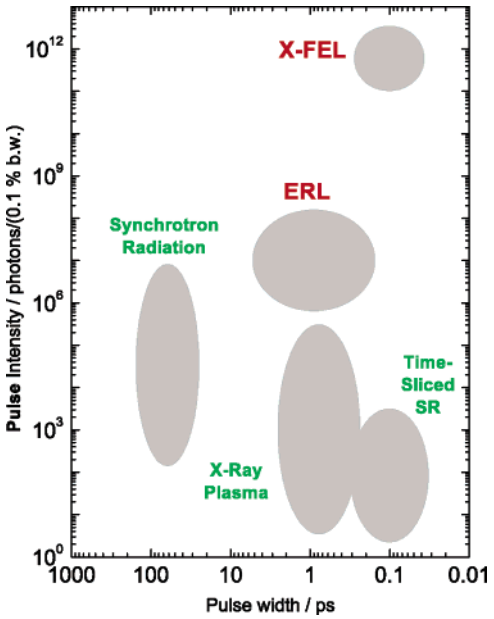

Figure 25. 25. Comparison of pulse intensities and time resolutions of present and future sources of subnanosecond-pulsed X-rays in the 2-20 keV range. Indicated is the number of X-ray photons per pulse (and 0.1 % bandwidth); thus, the repetition rate and the brightness of these sources are not accounted for.

tions of ≤100 fs. The idea of the X-FEL is to send the electrons down a very long (e.g., at LCLS, 120 m) undulator behind the linac to create a tunable, <200 fs X-ray pulse. By manipulating the energy levels of the electrons in the linac with the magnetic field of the undulator, one can tune the X-ray wavelength. The extremely long undulator allows X-ray photons, emitted by the electron bunches, to coherently build up, stimulating the emission of more X-ray photons, just as in a laser (which it actually is). The long undulator is essential because this laser "cavity" is mirrorless, thus giving rise to amplified spontaneous emission. When this beam is seeded into a second long undulator, the monochromatic output radiation intensity grows to unprecedented values, comparable to those of optical lasers, ca. $10^{11}-10^{12}$ per pulse, but with 3−4 orders of magnitude larger pulse energies. The TESLA Test Facility in Hamburg already produces scientific results in the XUV up to 100 eV on multiple ionization processes of rare gas clusters,[192] but the goal lies in generating ca. 10 keV radiation. The 3.7 km long TESLA facility in Hamburg and the 3 km long Linac Coherent Light Source at Stanford should come into operation around 2010 and 2008, respectively. An overview of the present and future sources of ultrashort X-ray sources in terms of flux and pulse duration is shown in Figure 25. Going beyond ultrafast XAS, the huge anticipated X-ray intensities from X-FELs will revolutionize many fields of science including plasma physics, condensed matter physics, chemistry, and biology. For example, single protein diffraction, rather than having to grow crystals, has been proposed.[219]

Beyond structural dynamics, one may ask what else the new X-ray sources, especially X-FELs, could be useful for. One area that we feel has a huge potential with the X-FEL is the field of nonlinear X-ray phenomena, which are the analogue to nonlinear optical phenomena. Optical spectroscopy is based on correlation functions of dipoles, and X-ray spectroscopy and X-ray scattering are based on the correlation functions of charge densities and of currents, respectively. Extending the formalisms and techniques of nonlinear optical methods to the X-ray domain,[220] as is being proposed by Mukamel and coworkers,[221−226] opens a whole new area of science, where one could look at electron−electron correlations and the flow of charges in a wide class of systems. Ultrafast X-ray absorption spectroscopy is the first step in this endeavor.

8. Acknowledgment

We would like to warmly thank our students and colleagues from the University of Lausanne and the Swiss Light Source in Villigen for their crucial contributions throughout our research in time-resolved XAS and for the many stimulating discussions: M. Saes, W. Gawelda, R. Abela, F. van Mourik, J. Helbing, D. Grolimund, A. Tarnovsky, M. Kaiser, P. Pattison, and B. Lang. We are also deeply grateful to our colleagues of the ALS-Berkeley and UC Berkeley, for their hospitality in providing us with the beamline and for their important backing and scientific stimulation: S. L. Johnson, P. A. Heimann, R. W. Schoenlein, M. Hertlein, A. Belkacem, A. M. Lindenberg, and R. W. Falcone. We also thank I. Kang and T. Missalla for their assistance during the early stages of this project at the ALS. We would also like to thank the following for their commitment to our time-resolved XAS projects: the Swiss Light Source (PSI-Villigen) and the Swiss NSF, via contract nos. 52561.97, 59146.99, and 620-66145.01.

9. References

(1) Zewail, A. H. *J. Phys. Chem. A* **2000**, *104*, 5660.
(2) Rosker, M. J.; Dantus, M.; Zewail, A. H. *J. Chem. Phys.* **1988**, *89*, 6113.
(3) Dantus, M.; Rosker, M. J.; Zewail, A. H. *J. Chem. Phys.* **1988**, *89*, 6128.
(4) Dhar, L.; Rogers, J. A.; Nelson, K. A. *Chem. Rev.* **1994**, *94*, 157.
(5) Garraway, B. M.; Suominen, K. A. *Rep. Progr. Phys.* **1995**, *58*, 365.
(6) Bowman, R. M.; Dantus, M.; Zewail, A. H. *Chem. Phys. Lett.* **1989**, *161*, 297.
(7) Gruebele, M.; Roberts, G.; Dantus, M.; Bowman, R. M.; Zewail, A. H. *Chem. Phys. Lett.* **1990**, *166*, 459.
(8) Rose, T. S.; Rosker, M. J.; Zewail, A. H. *J. Chem. Phys.* **1989**, *91*, 7415.
(9) Baumert, T.; Grosser, M.; Thalweiser, R.; Gerber, G. *Phys. Rev. Lett.* **1991**, *67*, 3753.
(10) Baumert, T.; Engel, V.; Rottgermann, C.; Strunz, W. T.; Gerber, G. *Chem. Phys. Lett.* **1992**, *191*, 639.
(11) Dantus, M.; Bowman, R. M.; Gruebele, M.; Zewail, A. H. *J. Chem. Phys.* **1989**, *91*, 7437.
(12) Chergui, M. *Femtochemistry ultrafast chemical and physical processes in molecular systems; World Scientific: Singapore, 1996.*
(13) Sundström, V. P., T.; van Grondelle, R. In *Femtochemistry and femtobiology ultrafast reaction dynamics at atomic-scale resolution Nobel Symposium 101, Bjèorkborn, Sweden, September 9−12, 1996*; Sundstrom, V., Ed.; Imperial College Press: London, 1997.
(14) Gaspard, P.; Instituts Solvay (Bruxelles) *Chemical reactions and their control on the femtosecond time scale XXth Solvay Conference on Chemistry*; Wiley: New York, 1997.
(15) Douhal, A. *Femtochemistry and femtobiology ultrafast dynamics in molecular science*; World Scientific: River Edge, NJ, 2002.
(16) Voth, G. A.; Hochstrasser, R. M. *J. Phys. Chem.* **1996**, *100*, 13034.
(17) Fleming, G. R. J., T.; Cho, M. In *Chemical reactions and their control on the femtosecond time scale XXth Solvay Conference*

on Chemistry; Gaspard, P., Instituts Solvay (Bruxelles), Eds.; Wiley: New York, 1997; Vol. 101.
(18) Apkarian, V. A.; Schwentner, N. *Chem. Rev.* **1999**, *99*, 1481.
(19) Chergui, M. *C. R. Acad. Sci., Ser. IV: Phys. Astrophys.* **2001**, *2*, 1453.
(20) Vigliotti, F.; Bonacina, L.; Chergui, M. *Phys. Rev. B* **2003**, *67*, art. no.-115118.
(21) Vigliotti, F.; Bonacina, L.; Chergui, M. *J. Chem. Phys.* **2002**, *116*, 4553.
(22) Jeannin, C.; Porrella-Oberli, M. T.; Jimenez, S.; Vigliotti, F.; Lang, B.; Chergui, M. *Chem. Phys. Lett.* **2000**, *316*, 51.
(23) Ye, X.; Demidov, A.; Wang, W.; Christian, J.; Champion, P. *Abstr. Papers Am. Chem. Soc.* **1998**, *216*, U778.
(24) Chen, T.; Engel, V.; Heid, M.; Kiefer, W.; Knopp, G.; Materny, A.; Meyer, S.; Pausch, R.; Schmitt, M.; Schwoerer, H.; Siebert, T. *J. Mol. Struct.* **1999**, *481*, 33.
(25) Williamson, J. C.; Zewail, A. H. *Proc. Natl. Acad. Sci. U.S.A.* **1991**, *88*, 5021.
(26) Williamson, J. C.; Dantus, M.; Kim, S. B.; Zewail, A. H. *Chem. Phys. Lett.* **1992**, *196*, 529.
(27) Williamson, J. C.; Zewail, A. H. *J. Phys. Chem.* **1994**, *98*, 2766.
(28) Dantus, M.; Kim, S. B.; Williamson, J. C.; Zewail, A. H. *J. Phys. Chem.* **1994**, *98*, 2782.
(29) Ihee, H.; Cao, J.; Zewail, A. H. *Chem. Phys. Lett.* **1997**, *281*, 10.
(30) Cao, J.; Ihee, H.; Zewail, A. H. *Chem. Phys. Lett.* **1998**, *290*, 1.
(31) Srinivasan, R.; Lobastov, V. A.; Ruan, C. Y.; Zewail, A. H. *Helv. Chim. Acta* **2003**, *86*, 1763.
(32) Goodson, B. M.; Ruan, C. Y.; Lobastov, V. A.; Srinivasan, R.; Zewail, A. H. *Chem. Phys. Lett.* **2003**, *374*, 417.
(33) Ihee, H.; Goodson, B. M.; Srinivasan, R.; Lobastov, V. A.; Zewail, A. H. *J. Phys. Chem. A* **2002**, *106*, 4087.
(34) Ihee, H.; Feenstra, J. S.; Cao, J. M.; Zewail, A. H. *Chem. Phys. Lett.* **2002**, *353*, 325.
(35) Ihee, H.; Cao, J. M.; Zewail, A. H. *Angew. Chem., Int. Ed.* **2001**, *40*, 1532.
(36) Cao, J. M.; Ihee, H.; Zewail, A. H. *Proc. Natl. Acad. Sci. U.S.A.* **1999**, *96*, 338.
(37) Trueblood, K. N.; Glusker, J. P. *Crystal structure analysis, a primer*, 2nd ed.; Oxford University Press: New York, 1985.
(38) Stout, G. H.; Stout, G. H.; Jensen, L. H.; Jensen, L. H. *X-ray structure determination a practical guide*, 2nd ed.; Wiley: New York, 1989.
(39) Rhodes, G. *Crystallography made crystal clear. A guide for users of macromolecular models*, 2nd ed.; Academic Press: San Diego, 2000.
(40) Rentzepis, P. M. *Time-resolved electron and X-ray diffraction 13−14 July 1995, San Diego, California*; SPIE: Bellingham, WA, 1995.
(41) BenNun, M.; Cao, J. S.; Wilson, K. R. *J. Phys. Chem. A* **1997**, *101*, 8743.
(42) Cao, J. S.; Wilson, K. R. *J. Phys. Chem. A* **1998**, *102*, 9523.
(43) Tomov, I. V.; Oulianov, D. A.; Chen, P. L.; Rentzepis, P. M. *J. Phys. Chem. B* **1999**, *103*, 7081.
(44) Debye, P. B., L.; Ehrhardt, F. *Phys. Zeitschr.* **1929**, *30*, 84.
(45) Chen, P.; Tomov, I. V.; Rentzepis, P. M. *J. Chem. Phys.* **1996**, *104*, 10001.
(46) Chen, P. L.; Tomov, I. V.; Rentzepis, P. M. *J. Phys. Chem. A* **1999**, *103*, 2359.
(47) Chen, P.; Tomov, I. V.; Rentzepis, P. M. *J. Appl. Crystallogr.* **1999**, *32*, 82.
(48) Larsson, J.; Judd, E.; Falcone, R. W.; Asfaw, A.; Lee, R. W.; Heimann, P. A.; Padmore, H. A.; Wark, J. *X-ray Lasers* **1996**, *1996*, 367.
(49) Larsson, J.; Heimann, P. A.; Lindenberg, A. M.; Schuck, P. J.; Bucksbaum, P. H.; Lee, R. W.; Padmore, H. A.; Wark, J. S.; Falcone, R. W. *Appl. Phys. A* **1998**, *66*, 587.
(50) Siders, C. W.; Cavalleri, A.; Sokolowski-Tinten, K.; Toth, C.; Guo, T.; Kammler, M.; von Hoegen, M. H.; Wilson, K. R.; von der Linde, D.; Barty, C. P. J. *Science* **1999**, *286*, 1340.
(51) Sokolowski-Tinten, K.; Blome, C.; Dietrich, C.; Tarasevitch, A.; von Hoegen, M. H.; von der Linde, D.; Cavalleri, A.; Squier, J.; Kammler, M. *Phys. Rev. Lett.* **2001**, *8722*, art. no.-225701.
(52) Cavalleri, A.; Siders, C. W.; Rose-Petruck, C.; Jimenez, R.; Toth, C.; Squier, J. A.; Barty, C. P. J.; Wilson, K. R.; Sokolowski-Tinten, K.; von Hoegen, M. H.; von der Linde, D. *Phys. Rev. B* **2001**, *6319*, art. no.-193306.
(53) Rose-Petruck, C.; Jimenez, R.; Guo, T.; Cavalleri, A.; Siders, C. W.; Raksi, F.; Squier, J. A.; Walker, B. C.; Wilson, K. R.; Barty, C. P. J. *Nature* **1999**, *398*, 310.
(54) Chin, A. H.; Schoenlein, R. W.; Glover, T. E.; Balling, P.; Leemans, W. P.; Shank, C. V. *Phys. Rev. Lett.* **1999**, *83*, 336.
(55) Lindenberg, A. M.; Kang, I.; Johnson, S. L.; Missalla, T.; Heimann, P. A.; Chang, Z.; Larsson, J.; Bucksbaum, P. H.; Kapteyn, H. C.; Padmore, H. A.; Lee, R. W.; Wark, J. S.; Falcone, R. W. *Phys. Rev. Lett.* **2000**, *84*, 111.
(56) Larsson, J.; Allen, A.; Bucksbaum, P. H.; Falcone, R. W.; Lindenberg, A.; Naylor, G.; Missalla, T.; Reis, D. A.; Scheidt, K.; Sjogren, A.; Sondhauss, P.; Wulff, M.; Wark, J. S. *Appl. Phys. A* **2002**, *75*, 467.
(57) Sokolowski-Tinten, K.; Blome, C.; Blums, J.; Cavalleri, A.; Dietrich, C.; Tarasevitch, A.; Uschmann, I.; Forster, E.; Kammler, M.; Horn-von-Hoegen, M.; von der Linde, D. *Nature* **2003**, *422*, 287.
(58) Cavalleri, A.; Toth, C.; Siders, C. W.; Squier, J. A.; Raksi, F.; Forget, P.; Kieffer, J. C. *Phys. Rev. Lett.* **2001**, *8723*, art. no.-237401.
(59) Rischel, C.; Rousse, A.; Uschmann, I.; Albouy, P. A.; Geindre, J. P.; Audebert, P.; Gauthier, J. C.; Forster, E.; Martin, J. L.; Antonetti, A. *Nature* **1997**, *390*, 490.
(60) Rousse, A.; Rischel, C.; Uschmann, I.; Forster, E.; Albouy, P. A.; Geindre, J. P.; Audebert, P.; Gauthier, J. C.; Antonetti, A. *J. Appl. Crystallogr.* **1999**, *32*, 977.
(61) Warren, B. E. *X-ray diffraction*; Addison-Wesley: Reading, MA, 1969.
(62) Zachariasen, W. H. *Theory on X-ray diffraction in crystals*, Repr. 1994 ed.; Dover: New York, 1994.
(63) Burgeat, J.; Taupin, D. *Acta Crystallogr. A* **1968**, *A 24*, 99.
(64) Wie, C. R.; Tombrello, T. A.; Vreeland, T. *J. Appl. Phys.* **1986**, *59*, 3743.
(65) Ma, H.; Lin, S. H.; Rentzepis, P. *J. Appl. Phys.* **1992**, *72*, 2174.
(66) Wulff, M.; Ursby, T.; Bourgeois, D.; Schotte, F.; Zontone, F.; Lorenzen, M. *J. Chim. Phys. Phys.-Chim. Biol.* **1996**, *93*, 1915.
(67) Perman, B.; Srajer, V.; Ren, Z.; Teng, T. Y.; Pradervand, C.; Ursby, T.; Bourgeois, D.; Schotte, F.; Wulff, M.; Kort, R.; Hellingwerf, K.; Moffat, K. *Science* **1998**, *279*, 1946.
(68) Techert, S.; Schotte, F.; Wulff, M. *Phys. Rev. Lett.* **2001**, *86*, 2030.
(69) Schotte, F.; Lim, M. H.; Jackson, T. A.; Smirnov, A. V.; Soman, J.; Olson, J. S.; Phillips, G. N.; Wulff, M.; Anfinrud, P. A. *Science* **2003**, *300*, 1944.
(70) Ohtaki, H.; Radnai, T. *Chem. Rev.* **1993**, *93*, 1157.
(71) Neutze, R.; Wouts, R.; Techert, S.; Davidsson, J.; Kocsis, M.; Kirrander, A.; Schotte, F.; Wulff, N. *Phys. Rev. Lett.* **2001**, *8719*, art. no.-195508.
(72) Bergsma, J. P.; Coladonato, M. H.; Edelsten, P. M.; Kahn, J. D.; Wilson, K. R.; Fredkin, D. R. *J. Chem. Phys.* **1986**, *84*, 6151.
(73) Bratos, S.; Mirloup, F.; Vuilleumier, R.; Wulff, M. *J. Chem. Phys.* **2002**, *116*, 10615.
(74) Rehr, J. J.; Albers, R. C. *Rev. Mod. Phys.* **2000**, *72*, 621.
(75) Messiah, A. *Quantum mechanics*, 9th ed.; North-Holland: Amsterdam, 1976.
(76) Bianconi, A. *EXAFS and near edge structure proceedings of the international conference Frascati, September 13−17, 1982*; Springer: Berlin, 1983.
(77) Bianconi, A. In *X-ray absorption principles, applications, techniques of exafs, sexafs and xanes*; Koningsberger, D. C. P., R., Ed.; Wiley: New York, 1988.
(78) Oyanagi, H. In *Applications of synchrotron radiation to material science*; Saisho, H. G., Y., Ed.; Elsevier Science B. V.: New York, 1996.
(79) Stern, E. A. H., S. M. In *Handbook on Synchrotron Radiation*; Eastman, D. E., Koch, E.-E., Eds.; North-Holland: Amsterdam, 1983; Vol. 1.
(80) de Groot, F. *Chem. Rev.* **2001**, *101*, 1779.
(81) Stern, E. A. *Phys. Rev. B* **1974**, *10*, 3027.
(82) Sayers, D. E.; Stern, E. A.; Lytle, F. W. *Phys. Rev. Lett.* **1971**, *27*, 1204.
(83) Bianconi, A.; Doniach, S.; Lublin, D. *Chem. Phys. Lett.* **1978**, *59*, 121.
(84) Bianconi, A. *Surf. Sci.* **1980**, *99*, 76.
(85) Belli, M.; Scafati, A.; Bianconi, A.; Mobilio, S.; Palladino, L.; Reale, A.; Burattini, E. *Solid State Commun.* **1980**, *35*, 355.
(86) Westre, T. E.; Kennepohl, P.; DeWitt, J. G.; Hedman, B.; Hodgson, K. O.; Solomon, E. I. *J. Am. Chem. Soc.* **1997**, *119*, 6297.
(87) Harris, D. C.; Bertolucci, M. D. *Symmetry and spectroscopy an introduction to vibrational and electronic spectroscopy*; Dover Publications: New York, 1989.
(88) Choy, J. H.; Kim, D. K.; Demazeau, G.; Jung, D. Y. *J. Phys. Chem.* **1994**, *98*, 6258.
(89) Choy, J. H.; Kim, D. K.; Hwang, S. H.; Demazeau, G.; Jung, D. Y. *J. Am. Chem. Soc.* **1995**, *117*, 8557.
(90) Choy, J. H.; Kim, J. Y.; Hwang, S. H.; Kim, S. J.; Demazeau, G. *Int. J. Inorg. Mater.* **2000**, *2*, 61.
(91) Ebbinghaus, S.; Hu, Z. W.; Reller, A. *J. Solid State Chem.* **2001**, *156*, 194.
(92) Dehmer, J. L. D., D. In *Electronic and atomic collisions: Proceedings of the XIth International Conference on the Physics of Electronic and Atomic Collisions, Kyoto, 29 August-4 September 1979: invited papers and progress reports*; Oda, N., Takayanagi, K., Eds.; Elsevier North-Holland, Inc.: New York, 1980.
(93) Lavilla, R. E.; Deslatte, Rd. *J. Chem. Phys.* **1966**, *44*, 4399.
(94) Dehmer, J. L. *J. Chem. Phys.* **1972**, *56*, 4496.
(95) Ferrett, T. A.; Lindle, D. W.; Heimann, P. A.; Kerkhoff, H. G.; Becker, U. E.; Shirley, D. A. *Phys. Rev. A* **1986**, *34*, 1916.
(96) Nakamatsu, H.; Mukoyama, T.; Adachi, H. *J. Chem. Phys.* **1991**, *95*, 3167.
(97) Sette, F.; Stohr, J.; Hitchcock, A. P. *Chem. Phys. Lett.* **1984**, *110*, 517.

(98) Sette, F.; Stohr, J.; Hitchcock, A. P. *J. Chem. Phys.* **1984**, *81*, 4906.
(99) Durham, P. J. In *X-ray absorption principles, applications, techniques of exafs, sexafs and xanes*; Koningsberger, D. C., Ed.; Wiley: New York, 1988.
(100) Fuggle, J. C.; Andrews, P. T. *Unoccupied electronic states fundamentals for XANES, EELS, IPS and BIS*; Springer: Berlin etc., 1992.
(101) de Groot, F. M. F.; Hu, Z. W.; Lopez, M. F.; Kaindl, G.; Guillot, F.; Tronc, M. *J. Chem. Phys.* **1994**, *101*, 6570.
(102) Stöhr, J. *NEXAFS spectroscopy*; Springer: Berlin, 1992.
(103) Krause, M. O. *J. Phys. Chem. Ref. Data* **1979**, *8*, 307.
(104) Hamalainen, K.; Siddons, D. P.; Hastings, J. B.; Berman, L. E. *Phys. Rev. Lett.* **1991**, *67*, 2850.
(105) Hayashi, H.; Udagawa, Y.; Caliebe, W. A.; Kao, C. C. *Chem. Phys. Lett.* **2003**, *371*, 125.
(106) Brown, F. L. H.; Wilson, K. R.; Cao, J. S. *J. Chem. Phys.* **1999**, *111*, 6238.
(107) Bressler, C. S., M.; Chergui, M.; Grolimund, D.; Abela, R. In *Femtochemistry and femtobiology ultrafast dynamics in molecular science*; Douhal, A., Ed.; World Scientific: River Edge, NJ, 2002.
(108) Bressler, C.; Saes, M.; Chergui, M.; Grolimund, D.; Abela, R.; Pattison, P. *J. Chem. Phys.* **2002**, *116*, 2955.
(109) Bressler, C.; Saes, M.; Chergui, M.; Abela, R.; Pattison, P. *Nucl. Instrum. Methods Phys. Res. Sect. A* **2001**, *467*, 1444.
(110) Saes, M. G., W.; van Mourik, F.; Lang, B.; Helbing, J.; Pattison, P.; Grolimund, D.; Abela, R.; Hertlein, M.; Belkacem, A.; Clover, T. E.; Heimann, P. A.; Schoenlein, R. W.; Johnson, S. L.; Lindenberg, A. M.; Kang, I.; Missalla, Th.; Falcone, R. W.; Chergui, M.; Bressler, Ch. *Rev. Sci. Instrum.* **2004**, *75*, 24.
(111) Saes, M. G., W.; Kaiser, M.; Tarnovsky, A.; Bressler, Ch.; Chergui, M.; Johnson, S. L.; Grolimund, D.; Abela, R. *Synchrotron Radiat. News* **2003**, *16* (4), 12.
(112) Egbert, A.; Chichkov, B. N.; Ostendorf, A. *Europhys. Lett.* **2001**, *56*, 228.
(113) Anderson, T.; Tomov, I. V.; Rentzepis, P. M. *J. Appl. Phys.* **1992**, *71*, 5161.
(114) Anderson, T.; Tomov, I. V.; Rentzepis, P. M. *J. Chem. Phys.* **1993**, *99*, 869.
(115) Tomov, I. V.; Anderson, T.; Rentzepis, P. M. *Appl. Phys. Lett.* **1992**, *61*, 3193.
(116) Tomov, I. V.; Anderson, T.; Rentzepis, P. M. *Appl. Phys. Lett.* **1992**, *61*, 1157.
(117) Tomov, I. V.; Chen, P.; Rentzepis, P. M. *Rev. Sci. Instrum.* **1995**, *66*, 5214.
(118) Helliwell, J. R.; Rentzepis, P. M. *Time-resolved diffraction*; Oxford University Press: New York, 1997.
(119) Derenzo, S. E.; Moses, W. W.; Blankespoor, S. C.; Ito, M.; Oba, K. *IEEE Trans. Nucl. Sci.* **1994**, *41*, 629.
(120) Girardeau-Montaut, J. P.; Kiraly, B.; Girardeau-Montaut, C.; Leboutet, H. *Nucl. Instrum. Methods Phys. Res. A* **2000**, *452*, 361.
(121) Norreys, P. A.; Zepf, M.; Moustaizis, S.; Fews, A. P.; Zhang, J.; Lee, P.; Bakarezos, M.; Danson, C. N.; Dyson, A.; Gibbon, P.; Loukakos, P.; Neely, D.; Walsh, F. N.; Wark, J. S.; Dangor, A. E. *Phys. Rev. Lett.* **1996**, *76*, 1832.
(122) Paul, A.; Bartels, R. A.; Tobey, R.; Green, H.; Weiman, S.; Christov, I. P.; Murnane, M. M.; Kapteyn, H. C.; Backus, S. *Nature* **2003**, *421*, 51.
(123) Bartels, R. A.; Paul, A.; Green, H.; Kapteyn, H. C.; Murnane, M. M.; Backus, S.; Christov, I. P.; Liu, Y. W.; Attwood, D.; Jacobsen, C. *Science* **2002**, *297*, 376.
(124) Lenzner, M.; Schnurer, M.; Spielmann, C.; Krausz, F. *IEICE Trans. Electron.* **1998**, *E81C*, 112.
(125) Spielmann, C.; Kan, C.; Burnett, N. H.; Brabec, T.; Geissler, M.; Scrinzi, A.; Schnurer, M.; Krausz, F. *IEEE J. Selected Top. Quantum Electron.* **1998**, *4*, 249.
(126) Drescher, M.; Hentschel, M.; Kienberger, R.; Tempea, G.; Spielmann, C.; Reider, G. A.; Corkum, P. B.; Krausz, F. *Science* **2001**, *291*, 1923.
(127) Hentschel, M.; Kienberger, R.; Spielmann, C.; Reider, G. A.; Milosevic, N.; Brabec, T.; Corkum, P.; Heinzmann, U.; Drescher, M.; Krausz, F. *Nature* **2001**, *414*, 509.
(128) Kitzler, M.; Milosevic, N.; Scrinzi, A.; Krausz, F.; Brabec, T. *Phys. Rev. Lett.* **2002**, *88*, art. no.-173904.
(129) Itatani, J.; Quere, F.; Yudin, G. L.; Ivanov, M. Y.; Krausz, F.; Corkum, P. B. *Phys. Rev. Lett.* **2002**, *88*, art. no.-173903.
(130) Kienberger, R.; Hentschel, M.; Uiberacker, M.; Spielmann, C.; Kitzler, M.; Scrinzi, A.; Wieland, M.; Westerwalbesloh, T.; Kleineberg, U.; Heinzmann, U.; Drescher, M.; Krausz, F. *Science* **2002**, *297*, 1144.
(131) Drescher, M.; Hentschel, M.; Kienberger, R.; Uiberacker, M.; Yakovlev, V.; Scrinizi, A.; Westerwalbesloh, T.; Kleineberg, U.; Heinzmann, U.; Krausz, F. *Nature* **2002**, *419*, 803.
(132) Baltuska, A.; Udem, T.; Uiberacker, M.; Hentschel, M.; Goulielmakis, E.; Gohle, C.; Holzwarth, R.; Yakoviev, V. S.; Scrinzi, A.; Hansch, T. W.; Krausz, F. *Nature* **2003**, *421*, 611.
(133) Nugent-Glandorf, L.; Scheer, M.; Samuels, D. A.; Mulhisen, A. M.; Grant, E. R.; Yang, X. M.; Bierbaum, V. M.; Leone, S. R. *Phys. Rev. Lett.* **2001**, *8719*, art. no.-193002.
(134) Nugent-Glandorf, L.; Scheer, M.; Samuels, D. A.; Bierbaum, V.; Leone, S. R. *Rev. Sci. Instrum.* **2002**, *73*, 1875.
(135) Nugent-Glandorf, L.; Scheer, M.; Samuels, D. A.; Bierbaum, V. M.; Leone, S. R. *J. Chem. Phys.* **2002**, *117*, 6108.
(136) Lei, C.; Bauer, M.; Read, K.; Tobey, R.; Liu, Y.; Popmintchev, T.; Murnane, M. M.; Kapteyn, H. C. *Phys. Rev. B* **2002**, *66*, art. no.-245420.
(137) Bauer, M.; Lei, C.; Read, K.; Tobey, R.; Gland, J.; Murnane, M. M.; Kapteyn, H. C. *Phys. Rev. Lett.* **2001**, *8702*, art. no.-025501.
(138) Murnane, M. M.; Kapteyn, H. C.; Falcone, R. W. *Phys. Fluids B* **1991**, *3*, 2409.
(139) Murnane, M. M.; Kapteyn, H. C.; Rosen, M. D.; Falcone, R. W. *Science* **1991**, *251*, 531.
(140) Kieffer, J. C.; Chaker, M.; Matte, J. P.; Pepin, H.; Cote, C. Y.; Beaudoin, Y.; Johnston, T. W.; Chien, C. Y.; Coe, S.; Mourou, G.; Peyrusse, O. *Phys. Fluids B* **1993**, *5*, 2676.
(141) Rousse, A.; Rischel, C.; Gauthier, J. C. *C. R. Acad. Sci. Ser. IV Phys. Astrophys.* **2000**, *1*, 305.
(142) Hatanaka, K.; Miura, T.; Fukumura, H. *Appl. Phys. Lett.* **2002**, *80*, 3925.
(143) Hatanaka, K.; Miura, T.; Odaka, H.; Ono, H.; Fukumura, H. *Bunseki Kagaku* **2003**, *52*, 373.
(144) Kieffer, J. C.; Dorchies, F.; Forget, P.; Gallant, P.; Jiang, Z.; Pepin, H.; Peyrusse, O.; Toth, C.; Cavalleri, A.; Squier, J.; Wilson, K. *Laser Phys.* **2001**, *11*, 1201.
(145) Kieffer, J. C.; Chien, C. Y.; Dorchies, F.; Forget, P.; Gallant, P.; Jiang, Z. M.; Pepin, H. *Acad. Sci. Ser. IV Phys. Astrophys.* **2000**, *1*, 297.
(146) Yu, J.; Jiang, Z.; Kieffer, J. C.; Krol, A. *Phys. Plasmas* **1999**, *6*, 1318.
(147) Von der Linde, D.; Sokolowski-Tinten, K.; Blome, C.; Dietrich, C.; Zhou, P.; Tarasevitch, A.; Cavalleri, A.; Siders, C. W.; Barty, C. P. J.; Squier, J.; Wilson, K. R.; Uschmann, I.; Forster, E. *Laser Particle Beams* **2001**, *19*, 15.
(148) Jiang, Y.; Lee, T. W.; Li, W.; Ketwaroo, G.; Rose-Petruck, C. G. *Opt. Lett.* **2002**, *27*, 963.
(149) Raksi, F.; Wilson, K. R.; Jiang, Z. M.; Ikhlef, A.; Cote, C. Y.; Kieffer, J. C. *J. Chem. Phys.* **1996**, *104*, 6066.
(150) Dohlus, M.; Limberg, T. *Nucl. Instrum. Methods Phys. Res. Sect. A* **1998**, *407*, 278.
(151) Schoenlein, R. W.; Chattopadhyay, S.; Chong, H. H. W.; Glover, T. E.; Heimann, P. A.; Shank, C. V.; Zholents, A. A.; Zolotorev, M. S. *Science* **2000**, *287*, 2237.
(152) Schoenlein, R. W.; Chong, H. H. W.; Glover, T. E.; Heimann, P. A.; Leemans, W. P.; Padmore, H. A.; Shank, C. V.; Zholents, A. A.; Zolotorev, M. S.; Corlett, J. S. *Acad. Sci. Ser. IV Phys. Astrophys.* **2001**, *2*, 1373.
(153) Schoenlein, R. W.; Chattopadhyay, S.; Chong, H. H. W.; Glover, T. E.; Heimann, P. A.; Leemans, W. P.; Shank, C. V.; Zholents, A.; Zolotorev, M. *Appl. Phys. B* **2000**, *71*, 1.
(154) Leemans, W.; Chattopadhyay, S.; Esarey, E.; Zholents, A.; Zolotorev, M.; Chin, A.; Schoenlein, R.; Shank, C. V. *Acad. Sci. Ser. IV Phys. Astrophys.* **2000**, *1*, 279.
(155) http://www2.slac.stanford.edu/tip/2003/aug15/bunches.htm.
(156) Maksimchuk, A.; Kim, M.; Workman, J.; Korn, G.; Squier, J.; Du, D.; Umstadter, D.; Mourou, G.; Bouvier, M. *Rev. Sci. Instrum.* **1996**, *67*, 697.
(157) Heimann, P. A.; Lindenberg, A. M.; Kang, I.; Johnson, S.; Missalla, T.; Chang, Z.; Falcone, R. W.; Schoenlein, R. W.; Glover, T. E.; Padmore, H. A. *Nucl. Instrum. Methods Phys. Res. Sect. A* **2001**, *467*, 986.
(158) Lindenberg, A. M.; Kang, I.; Johnson, S. L.; Falcone, R. W.; Heimann, P. A.; Chang, Z.; Lee, R. W.; Wark, J. S. *Optics Lett.* **2002**, *27*, 869.
(159) Murnane, M. M.; Kapteyn, H. C.; Falcone, R. W. *Appl. Phys. Lett.* **1990**, *56*, 1948.
(160) Larsson, J.; Chang, Z.; Judd, E.; Schuck, P. J.; Falcone, R. W.; Heimann, P. A.; Padmore, H. A.; Kapteyn, H. C.; Bucksbaum, P. H.; Murnane, M. M.; Lee, R. W.; Machacek, A.; Wark, J. S.; Liu, X.; Shan, B. *Opt. Lett.* **1997**, *22*, 1012.
(161) Johnson, S. L. H., P. A.; Lindenberg, A. M.; Jeschke, H. O.; Garcia, M. E.; Chang, Z.; Lee, R. W.; Rher, J. J.; Falcone, R. W. *Phys. Rev. Lett.* In press.
(162) Gallant, P.; Forget, P.; Dorchies, F.; Jiang, Z.; Kieffer, J. C.; Jaanimagi, P. A.; Rebuffie, J. C.; Goulmy, C.; Pelletier, J. F.; Sutton, M. *Rev. Sci. Instrum.* **2000**, *71*, 3627.
(163) Belzile, C.; Kieffer, J. C.; Cote, C. Y.; Oksenhendler, T.; Kaplan, D. *Rev Sci. Instrum.* **2002**, *73*, 1617.
(164) Matsushita, T.; Oyanagi, H.; Saigo, S.; Kaminaga, U.; Hashimoto, H.; Kihara, H.; Yoshida, N.; Fujimoto, M. *Jpn. J. Appl. Phys. Part 2—Lett.* **1986**, *25*, L523.
(165) Cohen, R. L.; Miller, G. L.; West, K. W. *Phys. Rev. Lett.* **1978**, *41*, 381.
(166) Rebane, K. K. *Impurity spectra of solids elementary theory of vibrational structure*; Plenum Press: New York, 1970.
(167) Chergui, M. *ChemPhysChem* **2002**, *8*, 713.

(168) Mills, D. M. *Acta Crystallogr. Sect. A* **1984**, *40*, C393.
(169) Mills, D. M. *Nucl. Instrum. Methods Phys. Res. Sect. A* **1984**, *222*, 159.
(170) Mills, D. M. *Phys. Today* **1984**, *37*, 22.
(171) Mills, D. M.; Lewis, A.; Harootunian, A.; Huang, J.; Smith, B. *Science* **1984**, *223*, 811.
(172) Mills, D. M.; Pollock, V.; Lewis, A.; Harootunian, A.; Huang, J. *Nucl. Instrum. Methods Phys. Res. Sect. A* **1984**, *222*, 351.
(173) Pollock, V.; Mills, D. M. *Nucl. Instrum. Methods Phys. Res. Sect. A* **1988**, *266*, 668.
(174) Clozza, A.; Castellano, A. C.; Dellalonga, S.; Giovannelli, A.; Bianconi, A. *Rev. Sci. Instrum.* **1989**, *60*, 2519.
(175) Chance, M. R.; Wirt, M. D.; Scheuring, E. M.; Miller, L. M.; Xie, A. H.; Sidelinger, D. E. *Rev. Sci. Instrum.* **1993**, *64*, 2035.
(176) Chance, B.; Fischetti, R.; Powers, L. *Biochemistry* **1983**, *22*, 3820.
(177) Powers, L.; Chance, B.; Chance, M.; Campbell, B.; Friedman, J.; Khalid, S.; Kumar, C.; Naqui, A.; Reddy, K. S.; Zhou, Y. *Biochemistry* **1987**, *26*, 4785.
(178) Chance, M. R.; Miller, L. M.; Fischetti, R. F.; Scheuring, E.; Huang, W. X.; Sclavi, B.; Hai, Y.; Sullivan, M. *Biochemistry* **1996**, *35*, 9014.
(179) Wang, H. X.; Peng, G.; Miller, L. M.; Scheuring, E. M.; George, S. J.; Chance, M. R.; Cramer, S. P. *J. Am. Chem. Soc.* **1997**, *119*, 4921.
(180) Chen, L. X.; Lee, P. L.; Gosztola, D.; Svec, W. A.; Montano, P. A.; Wasielewski, M. R. *J. Phys. Chem. B* **1999**, *103*, 3270.
(181) Thiel, D. J.; Livins, P.; Stern, E. A.; Lewis, A. *Nature* **1993**, *362*, 40.
(182) Thiel, D. J.; Livins, P.; Stern, E. A.; Lewis, A. *Nature* **1993**, *363*, 565.
(183) Petkov, V.; Takeda, S.; Waseda, Y.; Sugiyama, K. *J. Non-Cryst. Solids* **1994**, *168*, 97.
(184) Murakami, K.; Gerritsen, H. C.; Vanbrug, H.; Bijkerk, F.; Saris, F. W.; Vanderwiel, M. J. *Phys. Rev. Lett.* **1986**, *56*, 655.
(185) Murakami, K. O., T.; Miyashita, A.; Yoda, O. *AIP Conf. Proc.* **1994**, *228*, 375.
(186) Chen, L. X.; Jager, W. J. H.; Jennings, G.; Gosztola, D. J.; Munkholm, A.; Hessler, J. P. *Science* **2001**, *292*, 262.
(187) Chen, L. X. *J. Electron Spectrosc. Relat. Phenom.* **2001**, *119*, 161.
(188) Chen, L. X.; Jennings, G.; Liu, T.; Gosztola, D. J.; Hessler, J. P.; Scaltrito, D. V.; Meyer, G. J. *J. Am. Chem. Soc.* **2002**, *124*, 10861.
(189) Jennings, G.; Jager, W. J. H.; Chen, L. X. *Rev. Sci. Instrum.* **2002**, *73*, 362.
(190) Hudson, E.; Shirley, D. A.; Domke, M.; Remmers, G.; Puschmann, A.; Mandel, T.; Xue, C.; Kaindl, G. *Phys. Rev. A* **1993**, *47*, 361.
(191) Oguri, K.; Nakano, H.; Nishikawa, T.; Uesugi, N. *Appl. Phys. Lett.* **2001**, *79*, 4506.
(192) Wabnitz, H.; Bittner, L.; de Castro, A. R. B.; Dohrmann, R.; Gurtler, P.; Laarmann, T.; Laasch, W.; Schulz, J.; Swiderski, A.; von Haeften, K.; Moller, T.; Faatz, B.; Fateev, A.; Feldhaus, J.; Gerth, C.; Hahn, U.; Saldin, E.; Schneidmiller, E.; Sytchev, K.; Tiedtke, K.; Treusch, R.; Yurkov, M. *Nature* **2002**, *420*, 482.
(193) Siffalovic, P.; Drescher, M.; Spieweck, M.; Wiesenthal, T.; Lim, Y. C.; Weidner, R.; Elizarov, A.; Heinzmann, U. *Rev. Sci. Instrum.* **2001**, *72*, 30.
(194) Bauer, M.; Aeschlimann, M. *J. Electron Spectrosc. Relat. Phenom.* **2002**, *124*, 225.
(195) Schmidt, O.; Bauer, M.; Wiemann, C.; Porath, R.; Scharte, M.; Andreyev, O.; Schonhense, G.; Aeschlimann, M. *Appl. Phys. B* **2002**, *74*, 223.
(196) Lemell, C.; Tong, X. M.; Krausz, F.; Burgdorfer, J. *Phys. Rev. Lett.* **2003**, *90*, art. no.-076403.
(197) Balmer, J.; Lewis, C. L. S.; Corbett, R. E.; Robertson, E.; Saadat, S.; Oneill, D.; Kilkenny, J. D.; Back, C. A.; Lee, R. W. *Phys. Rev. A* **1989**, *40*, 330.
(198) Davidson, S. J.; Foster, J. M.; Smith, C. C.; Warburton, K. A.; Rose, S. J. *Appl. Phys. Lett.* **1988**, *52*, 847.
(199) Probst, M.; Haight, R. *Appl. Phys. Lett.* **1997**, *71*, 202.
(200) Ankudinov, A. L.; Ravel, B.; Rehr, J. J.; Conradson, S. D. *Phys. Rev. B* **1998**, *58*, 7565.
(201) Johnson, S. L. Thesis, University of California, 2002.
(202) Adams, B. W.; DeCamp, M. F.; Dufresne, E. M.; Reis, D. A. *Rev. Sci. Instrum.* **2002**, *73*, 4150.
(203) Saes, M.; Bressler, C.; Abela, R.; Grolimund, D.; Johnson, S. L.; Heimann, P. A.; Chergui, M. *Phys. Rev. Lett.* **2003**, *90*, art. no.-047403.
(204) Juris, A.; Balzani, V.; Barigelletti, F.; Campagna, S.; Belser, P.; Vonzelewsky, A. *Coord. Chem. Rev.* **1988**, *84*, 85−277.
(205) Gray, H. B. In *Electron transfer in chemistry*; Balzani, V., Ed.; Wiley-VCH: Weinheim, 2001.
(206) Damrauer, N. H.; Cerullo, G.; Yeh, A.; Boussie, T. R.; Shank, C. V.; McCusker, J. K. *Science* **1997**, *275*, 54.
(207) Yeh, A. T.; Shank, C. V.; McCusker, J. K. *Science* **2000**, *289*, 935.
(208) Sham, T. K. *J. Chem. Phys.* **1985**, *83*, 3222.
(209) Sugiura, C.; Kitamura, M.; Muramatsu, S. *J. Chem. Phys.* **1986**, *84*, 4824.
(210) Saes, M. G., W.; Kaiser, M.; Tarnovsky, A.; Bressler, Ch.; Chergui, M.; Johnson, S. L.; Grolimund, D.; Abela, R. *Chem. Phys.* Submitted.
(211) Chen, L. X.; Shaw, G. B.; Novozhilova, I.; Liu, T.; Jennings, G.; Attenkofer, K.; Meyer, G. J.; Coppens, P. *J. Am. Chem. Soc.* **2003**, *125*, 7022.
(212) Rousse, A. Private communication 2003.
(213) Tigner, M. *Nuovo Cimento* **1965**, *37*, 1228.
(214) Gruner, S. M.; Bilderback, D. H. *Nucl. Instrum. Methods Phys. Res. Sect. A* **2003**, *500*, 25.
(215) Gruner, S. M.; Bilderback, D.; Bazarov, I.; Finkelstein, K.; Krafft, G.; Merminga, L.; Padamsee, H.; Shen, Q.; Sinclair, C.; Tigner, M. *Rev. Sci. Instrum.* **2002**, *73*, 1402.
(216) Corlett, J. N. W. A. B.; De Santis, S.; Doolittle, L.; Fawley, W. M.; Green, M. A.; Leone, P. H., S.; Lidia, S.; Li, D.; Ratti, A. K.; Robinseon, R. S.; Staples, J.; Wan, W.; Wells, R.; Wolski, A.; Zholents, A. Particle Accelerator Conference, Portland, Oregon, 2003.
(217) http://erl.chess.cornell.edu/.
(218) http://www-als.lbl.gov/als/20/LUXtext.html.
(219) Neutze, R.; Wouts, R.; van der Spoel, D.; Weckert, E.; Hajdu, J. *Nature* **2000**, *406*, 752.
(220) Mukamel, S. *Principles of nonlinear optical spectroscopy*; Oxford University Press: New York, 1995.
(221) Tanaka, S.; Mukamel, S. *Phys. Rev. A* **2003**, *67*, art. no.-033818.
(222) Tanaka, S.; Volkov, S.; Mukamel, S. *J. Chem. Phys.* **2003**, *118*, 3065.
(223) Tanaka, S.; Mukamel, S. *Phys. Rev. Lett.* **2002**, *89*, art. no.-043001.
(224) Tanaka, S.; Mukamel, S. *J. Chem. Phys.* **2002**, *116*, 1877.
(225) Tanaka, S.; Mukamel, S. *Phys. Rev. A* **2001**, *6403*, art. no.-032503.
(226) Tanaka, S.; Chernyak, V.; Mukamel, S. *Phys. Rev. A* **2001**, *6306*, art. no.-063405.

CR0206667